

Chapter 1

Introduction to Laser-Assisted Fabrication of Materials

Jyotsna Dutta Majumdar and Indranil Manna

Abstract Light amplification by stimulated emission of radiation (laser) is a coherent and monochromatic source of electromagnetic radiation that can propagate in a straight line and hence, finds diverse applications. High power lasers can perform various manufacturing operations or material processing. This contribution provides the principle of laser materials processing and an overview of the engineering application of laser material processing. The manufacturing processes covered have been broadly divided into four major categories; namely, laser assisted forming, joining, machining, and surface engineering. Followed by a brief introduction to different types of lasers and their general application, fundamentals of laser–matter interaction and classification of laser material processing have been provided. The scope and principle of an individual process is described followed by a detailed update of the literature, scientific issues, and technological innovations. The entire discussion primarily focuses on correlating the properties with processing parameters and microstructure and composition.

1.1 Introduction

Laser, the acronym of light amplification by stimulated emission of radiation is a coherent and monochromatic source of electromagnetic radiation with wavelength ranging from the ultraviolet to the infrared range [1–4]. Lasers can deliver very

J. D. Majumdar (✉) · I. Manna
Metallurgical and Materials Engineering Department,
Indian Institute of Technology, Kharagpur 721 302, West Bengal, India
e-mail: jyotsna@metal.iitkgp.ernet.in

I. Manna
Central Glass and Ceramic Research Institute,
Kolkata 700 032, West Bengal, India
e-mail: imanna@metal.iitkgp.ernet.in

low (\sim mW) to extremely high (1–100 kW) focused power with a precise spot size/dimension and spatial/temporal distribution on a given substrate through any intervening medium [1–4]. As a result, lasers have wide-ranging applications in different materials processing [5, 6].

The initial foundation of the laser theory was laid by Einstein [7]. Subsequently, Kopfermann and Ladenburg [8] presented the first experimental confirmation of Einstein's prediction. In 1960, Maiman [9] invented the first working ruby laser for which he was awarded the Nobel Prize. Subsequently, several new lasers including semiconductor lasers, Nd:YAG lasers, CO₂ gas lasers, dye lasers, and other types of gas lasers were designed and fabricated with better reliability and durability. By the mid 1970s, more reliable and powerful lasers were developed for industrial applications such as cutting, welding, drilling, and melting. During the 1980s and early 1990s, lasers were successfully applied for heating, cladding, alloying, glazing, and thin film deposition.

Depending on the type of laser and wavelength desired, the laser medium could be solid, liquid, or gaseous. Different laser types are commonly named according to the state or the physical properties of the active medium. Consequently, there are glass or semiconductor, solid state, liquid, and gas lasers. Gas-based lasers can be further subdivided into neutral atom lasers, ion lasers, molecular lasers, and excimer lasers. The typical commercially available lasers are (a) solid state or glass laser (Nd:YAG, Ruby), (b) semiconductor or diode laser (AlGaAs, GaAsSb and GaAlSb), (c) dye or liquid lasers (solutions of dyes in water/alcohol and other solvents), (d) neutral or atomic gas lasers (He–Ne, Cu or Au vapour), (e) ion lasers [argon (Ar⁺) and krypton (Kr⁺) ion], (f) molecular gas lasers (CO₂ or CO), and (g) excimer laser (XeCl, KrF). The wavelengths of the presently available lasers cover a wide spectral range from the far infrared to the soft X-ray.

1.2 Principle, Type, and Application of Laser

Laser comprises three principal components, namely, a gain medium, a device for exciting the gain medium, and an optical delivery/feedback system. Additional provisions of cooling the mirrors, guiding the beam, and manipulating the target are necessary to facilitate material processing. Figure 1.1 schematically shows the operating principle of a CO₂ laser. As illustrated in Fig. 1.1a, the laser device consists of three main parts: a gain or laser medium CO₂, an optical resonator or cavity with two mirrors (mirror 1 and 2, placed at opposite ends), and an energizing or pumping source that supplies energy to the gain medium to activate CO₂ into amplifying state [10]. The chemical species in the gain medium (composition, bond energy, band gap, etc.) determines the wavelength of the optical output. Between the two mirrors, one is a fully reflecting and the other a partially reflecting one. From the quantum mechanical principle, when an external energy is supplied to an atom/molecule, the irradiated species attains an excited or higher energy state (E_2) only to spontaneously and instantaneously return to the ground state (E_1) by emitting the energy difference

as a photon of frequency (ν):

$$\nu = (E_2 - E_1)/h, \quad (1.1)$$

Where, h is the Planck's constant. This phenomenon is known as spontaneous emission, which subsequently may excite another atom and stimulate it to emit a photon by de-exciting it to a lower energy level through a process called stimulated emission of radiation. This process in the initial stage occurs randomly and can multiply itself (Fig. 1.1b). However, the emitted radiation is coherent with the stimulating source so that the wavelength, phase, and polarization between the two are identical. A photon interacting with a ground state atom may get absorbed in order to excite it to a higher energy state. This situation, called 'population inversion' is created by the pumping source. The photons moving along the optical axis interact with a large number of excited atoms, stimulate them and in the process get amplified. They are reflected back and forth by the resonator mirrors and pass through the excited medium creating more photons. In each of these cycles, a percentage of these photons exit through the partially transmitting mirror as intense laser beam (Fig. 1.1c). Finally, the laser beam is guided on to the workpiece by using reflecting mirrors and prisms. Instead of CO_2 , the active medium could be a solid (e.g. Nd:YAG or neodymium doped yttrium–aluminium–garnet), liquid (dye) or another gas (e.g. He, Ne, etc.). In addition, there is the free-electron laser, which exploits a beam of accelerated electron moving through a magnetic assembly (modulator) as an active medium to generate a periodic magnetic field. For a ready reference, the characteristic features of some commonly used lasers, other than CO_2 laser, will now be outlined in brief.

1.2.1 Solid-State Laser

One of the most commonly used solid-state lasers is based on neodymium doped yttrium aluminium garnet (Nd:YAG) [11]. Here, neodymium atom is utilized in its trivalent state in the yttrium aluminium garnet crystal ($\text{Y}_3\text{Al}_5\text{O}_{12}$ or YAG). The excitation is accomplished by irradiating the material by a flash and arc lamp. The output power of this laser for continuous wave operation is in the range of a few watts up to a few kW. The output energies for pulsed lasers range from a few mJ to a few tens of Joules. The total efficiency is around 2%. Nd:YAG laser is commonly used for materials processing (cutting, drilling, welding, marking, surface engineering), medical (endoscopic surgery), and military (long range finders) applications. The major advantages of Nd:YAG laser over CO_2 laser lie in its smaller wavelength (1.06 μm) and ability to deliver laser radiation through optical fibers. To increase the overall efficiency, attempts are being made to introduce new active materials containing sensitizer atoms to increase the overall efficiency of laser by absorbing the larger fraction of pump radiation and transferring it to active atom.

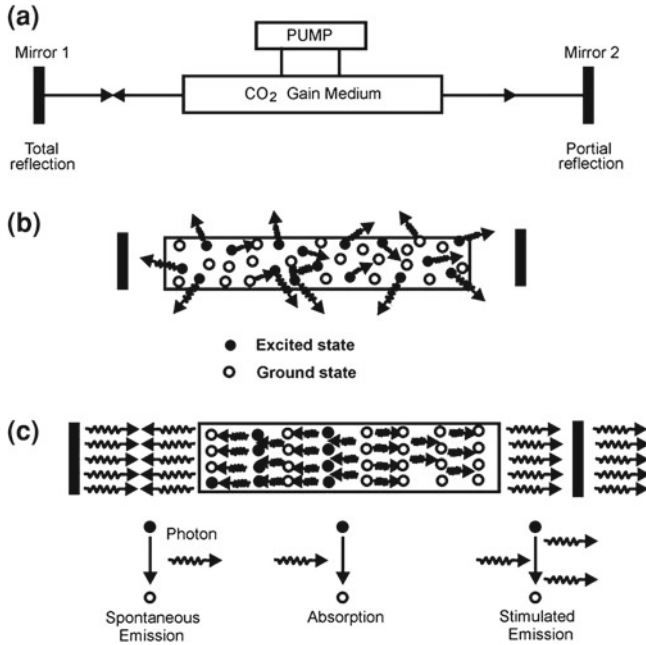


Fig.1.1 Schematic setup showing generation of laser (a) the major constituents of the machine, (b) excitation and de-excitation of the atoms in the medium, and (c) stimulated emission and formation of laser beam [10]

1.2.2 Semiconductor or Diode Lasers

Laser action in GaAs and GaAsP laser diodes at cryogenic temperature was demonstrated as early as 1962 [11, 12]. The application of diode laser in that period was limited by the poor output power. However, these semiconductor lasers are now becoming increasingly popular both as a pump source for solid-state laser and in materials processing because of their unique features like small size, low weight, high efficiency, and reliability. More frequently used diodes are based on double hetero-junction using ternary compounds such as AlGaAs (p) and GaAs/GaAlAs (n). In this type of laser, the emitted radiation comes from the stimulated emission resulting from the recombination of electrons in the conduction band with holes in the valence band. However, several diode bars mounted into the multi-channel heat sinks are stacked on top of each other to further increase the power. Diode lasers have a potential scope of application in materials processing and gaining increasing popularity because of its lower installation/ maintenance cost and greater efficiency over CO₂ and Nd:YAG lasers [13].

1.2.3 Gas-Based Lasers

As already stated, CO₂ lasers seem to be one of the earliest developed and most popular lasers among the commercially available lasers for material processing because they are electrically more efficient (15–20%) and produce higher powers (0.1–50 kW) than other lasers in the continuous mode [14]. Despite being less efficient in energy coupling with metals due to longer wavelength (10.6 μm), the higher wall plug (~ 12%) and quantum (~ 45%) efficiency along with higher level of output power of CO₂ lasers more than compensate for the poor laser–matter energy coupling capability. On the other hand, Nd:YAG and Ruby lasers possess shorter wavelength and are more suited to pulsed mode of applications requiring deeper penetration, smaller area coverage, and precision treatment of materials for specific purposes. However, sheer size/volume of the CO₂ laser unit and operational/maintenance complexities are major disadvantages that have contributed in shifting attention toward solid-state lasers.

1.2.4 Free-Electron Lasers

Free-electron lasers are capable of operation over the entire electromagnetic spectrum from the microwave to the vacuum ultraviolet regions at average powers up to several kilowatts and peak powers up to a gigawatt [15]. At present, there are two principal areas for future free-electron laser development: higher average power and shorter wavelengths. Free-electron lasers consist of an electron beam propagating through a periodic magnetic field, called a wiggler or undulator [15]. Undulators are also used in incoherent synchrotron light sources. Lasing occurs because the wiggler and radiation combine to produce a heat wave that travels slower than the speed of light and can be synchronous with the electrons. The free-electron laser is continuously tunable, capable of high peak and average powers, and can produce a wide variety of pulse formats. The average power of this laser can be further raised. In continuous mode, a record average power of 1.7 kW has been produced at a wavelength of 3 μm. Similar power levels of about 2 kW in 1 ms pulse have also been produced in the infrared region. The high average power goal is several tens of kilowatts at infrared to ultraviolet wavelengths. The most likely configuration for generating a free-electron laser is an oscillator driven by a radiofrequency linear accelerator.

1.2.5 Ultra High Field Lasers

The development of lasers that are capable of producing short pulses of very high power has progressed enormously over the past 10 years [13]. There are two main types of ultra high field lasers in common use. On account of its broad gain bandwidth, Ti:sapphire (TiS) lasers enable pulses of very short durations (few tens of

femtoseconds) to be produced and energies of up to 1 J can be achieved at relatively high repetition rates (typically 10 Hz). Higher energy pulses (with a focused intensity of 10^{25} W/m²) can be obtained from Nd:glass lasers with a longer (several hundred femtoseconds) pulse durations and lower repetition rates [16, 17].

1.2.6 Excimer Lasers

Gas lasers make use of unstable molecules as the active material that is formed within the same electrical discharge used for the excitation. These molecules originate from the association of noble gas atoms such as Ar, Kr, Xe with halogen atoms such as F, Cl, Br. The available average power can reach the few hundred watts level in commercial units with an energy per pulse of the order of one joule and pulse repetition frequencies in the 100 Hz range. The achievable efficiencies can reach 4%, and the use of corrosion resistant materials has improved the discharge tube lifetime. These lasers are used for spectroscopy and photochemistry experiments in the ultraviolet range and for many applications related to surface treatment.

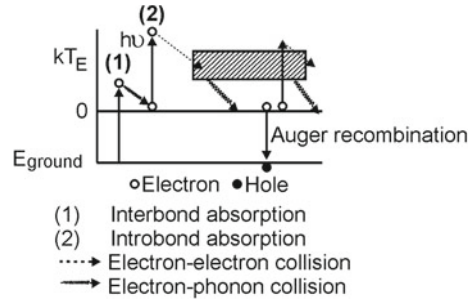
1.3 Laser–Matter Interaction for Material Processing

Laser–matter interaction within the near-surface region achieves extreme heating and cooling rates (10^3 – 10^{10} K/s), while the total deposited energy (typically, 0.1–10 J/cm²) is insufficient to affect, in a significant way, the temperature of the bulk material. This allows the near-surface region to be processed under extreme conditions with little effect on the bulk properties.

1.3.1 Lattice Heating

The initial stage in all laser assisted material processing applications involves the coupling of laser radiation to electrons within the metal. Initially, this occurs by the absorption of photons from the incident laser beam promoting the electrons from the valence/conduction bands to states of higher energy. Electrons that have been excited in this manner can divest themselves of their excess energy in a variety of ways. For example, if the photon energy is large enough ($>$ several eV), the excited electrons can be removed entirely from the metal, causing the photoelectric effect. Most laser processing applications, however, utilize lasers emitting photons with relatively low energy. The energy of CO₂ laser photons is only 0.12 eV while the photons obtained from the Nd:YAG laser have about 1.2 eV of energy. Electrons excited by absorption of CO₂ or Nd:YAG laser radiation does not therefore have enough energy to be ejected from the metal surface. Such electrons must,

Fig.1.2 Schematic diagram depicting electron excitation and carrier relaxation process in solids subjected to intense laser irradiation [18]



nevertheless, lose energy to return to an equilibrium state after photon excitation. This occurs when excited electrons are scattered by lattice defects like non-crystalline regions in a crystal such as dislocations and grain boundaries. In either case, the overall effect is to convert electronic energy derived from the beam of incident photons into heat. It is this heat that is useful (indeed necessary) in all material processing applications.

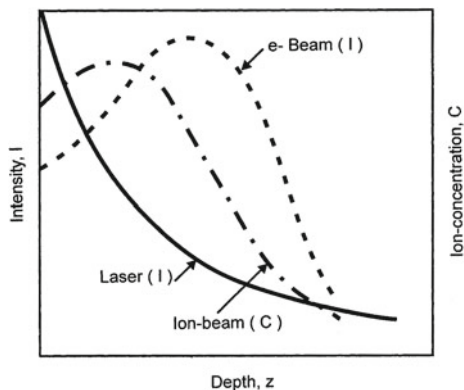
Figure 1.2 summarizes the process of electron excitation and excited carrier relaxation involved during laser–matter interaction schematically [18]. Photon interaction with matter occurs usually through the excitation of valence and conduction band electrons throughout the wavelength band from infrared (10 μm) to ultraviolet (0.2 μm) region. Absorption of wavelength between 0.2–10 μm leads to intraband transition (free electrons only) in metals and interband transition (valence to conduction) in semiconductors. Conversion of the absorbed energy to heat involves (a) excitation of valence and/or conduction band electrons, (b) excited electron–phonon interaction within a span of 10^{-11} – 10^{-12} s, (c) electron–electron or electron–plasma interaction, and (d) electron–hole recombination within 10^{-9} – 10^{-10} s (Auger-process). Since free carrier absorption (by conduction band electrons) is the primary route of energy absorption in metals, beam energy is almost instantaneously transferred to the lattice by electron–phonon interaction. Similarly, transition in semiconductor or polymers having ionic/covalent bonding with energy gap between conduction and valence bands is marginally slower.

1.3.2 Spatial Distribution of Deposited Energy

The spatial profile of deposited energy from laser beam is illustrated in Fig. 1.3. The laser beam intensity I at a depth z for the normally incident beam of initial intensity I_0 is given by [18]

$$I(z, t) = I_0(t)(1 - R)\exp(-\alpha z). \quad (1.2)$$

Fig.1.3 Spatial profile of deposited energy intensity (I) or concentration (C) with depth (z) following irradiation/implantation of solid matter by laser, electron, and ion beams, respectively [18]



Here, I_0 is the incident intensity, t is time, R and α are the reflectivity and absorption coefficient, respectively. Since α is very high ($\sim 10^8 \text{ m}^{-1}$) for metals, light is totally absorbed within a depth of 10–20 nm. The efficiency of optical coupling is determined by the reflectivity (R). R for metals is relatively low at short wavelengths, rises abruptly at a critical wavelength, then remains very high at long wavelength [18].

For comparison, the deposited energy profile from the other two important directed-energy-sources, namely electron and ion beams, are also shown in Fig. 1.3. The energy deposition profile for electron beam irradiation of matter is given by a Gaussian function,

$$I(z, t) = I_0(t)(1 - R_E)f_E(x/x_P) \quad (1.3)$$

Here, R_E is the reflectivity for electron beam, x_P is the distance (x) that coincides with the peak intensity, and $f_E(x/x_P)$ is the spatial energy deposition profile. The deposition profile depends on the energy loss, hence on incident energy and atomic number. Thus, electron beam is more suited to deep penetration welding than to surface engineering applications. The concentration (C) of the implanted species in ion beam irradiation does not coincide with the top surface but lies underneath the surface as follows:

$$C(z) = \frac{Q_T}{\sqrt{2\pi} \Delta R_P} \exp \left[- \left(\frac{z - R_P}{\sqrt{2} \Delta R_P} \right)^2 \right] \quad (1.4)$$

Here, $C(z)$ is the concentration of a given species at a vertical distance z , R_P is the projected range/distance and Q_T is the ion dose.

1.3.3 Heat Transfer by Laser Irradiation

Usually, the deposited energy of laser irradiation is converted into heat on a timescale shorter than the pulse duration or laser interaction time [18]. The resulting

temperature profile depends on the deposited energy profile and thermal diffusion rate during laser irradiation. Thermal diffusivity (D) is related to thermal conductivity (k) and specific heat (c_p) as follows:

$$D = k / (\rho c_p) \quad (1.5)$$

where, ρ is the density. The vertical distance (z) over which heat diffuses during the pulse duration (t_p) is given by, $z = (2Dt_p)^{1/2}$. Here, z in comparison to laser absorption depth (α^{-1}) determines the temperature profile. For laser irradiation of metals, the typical value of α^{-1} is much less than z .

Under the one-dimensional heat flow condition, the heat balance can be expressed as [6]:

$$\rho c_p \frac{\partial T(z, t)}{\partial t} = Q(z, t) + \frac{\partial}{\partial z} k \frac{\partial T(z, t)}{\partial z} \quad (1.6)$$

where, T and Q are the temperature and power density at a given vertical distance of depth (z) and time (t), respectively. Q follows the functional relation with z as in Eq. (1.2). The heat balance Eq. (1.6) may be solved analytically if the coupling parameters (α and R) and materials parameters (ρ , k and c_p) are not temperature and phase dependent. However, phase changes are unavoidable except in solid-state processing. Thus, the heat balance equation is solved by numerical techniques like finite difference/element or controlled volume methods.

Depending on the temperature profile, the irradiated material may undergo only heating, melting, or vaporization. For surface melting and subsequent re-solidification, the solid–liquid interface initially moves away from and then travels back to the surface with a velocity as high as 1–30 m/s. The interface velocity is given by $v \propto (T_m - T_i)$, where T_m and T_i are the melting and interface temperatures, respectively [18]. Further details on mathematical modeling of heat transfer and phase evolution in laser material processing may be obtained in several textbooks dealing with laser material processing [4–6, 18].

1.3.4 Plasma Formation During Laser Irradiation

Laser-driven processes in which vaporization takes place are important for many applications like laser drilling and cutting, laser-induced surface chemical reactions in the reactive atmospheres, etc. [16, 19]. What is common to all these diverse applications of laser is the formation of a charged vapor stream. The ionized vapor contains not only the electrons and simple ions (as usually understood in a simple picture) but also the clusters of metals, reacted particles of oxides, nitrides, etc., which are charged and behave as Coulomb particles. They may form very complex structures of Coulomb liquids and solids, and show some new effects. Such plasma, called ‘dusty’ or ‘colloidal’ plasma has been considered in many studies [20]. Chu and Lin

[21], Melzer et al. [22], and Piel and Melzer [23] presented direct evidence of generation of plasma during laser-induced vaporization. Gnedovets et al. [24] synthesized ultrafine particles by laser vaporization of materials (metals, metal oxides, carbon) in a high-pressure atmosphere of chemically active (hydrogen, oxygen, air) and inert (helium, argon, xenon) gases as a result of vapor condensation. The dimensions of particles increased with increasing the ambient gas pressure. A particle nucleation and growth theory is used to describe the formation of the dispersed condensate in the erosive plasma. Cauble et al. [25] showed that the particle size, the particle–particle distance, and the particle density developed by laser assisted vaporization technique would depend on the laser power, gas pressure, and evaporation rate (i.e. on the boiling point of the material). Moreover, the vapor particle size should decrease with decreasing pressure and evaporation rate [26].

1.3.5 Effect of Ultra High Power Laser Irradiation

At very high intensities, the interaction between the radiation and matter gives rise to quite different phenomena from that observed at lower intensities [16]. For example, the energy acquired by an electron driven by the very high oscillating electric field of the intense radiation is approximately 10 MeV for laser intensity of 10^{24} W/m². Electrons with this energy can produce Bremsstrahlung or continuous radiation in the γ -ray range that is sufficiently energetic to induce (γ , n) nuclear reactions. Electrons can be accelerated to 100 MeV by plasma waves created by intense laser pulses and these interactions can also give rise to beams of energetic protons with applications in time-resolved imaging and tomography. Ultra high field lasers have been used to compress materials to ultra-high pressures and characterize their thermodynamic and transport properties [26]. When an ultra-high power laser pulse is focused into dense plasma, magnetic fields up to 10^9 G are generated and this has been predicted by both computer simulations and analytical calculations [16]. These fields are predicted to be localized near the critical density surface, i.e., the region where the laser frequency equals the plasma frequency and where most of the laser absorption takes place.

1.4 Application of Laser

Figure 1.4 presents a brief overview of the application of lasers in different fields with diverse objectives [2]. The list is neither complete nor exhaustive but is meant for providing an overview with representative examples. It serves only to show the diversity of the application of laser. In some applications, the power output is of main concern, e.g. atomic fusion and isotope separation. Sometimes, the main reason for using laser lies in spectral purity and coherence (pollution detection, length/velocity measurement, interferometry, etc.), low divergence (laser show, pointer/guide, audio-player), or a combination of all of them (communication, holography, metrology).

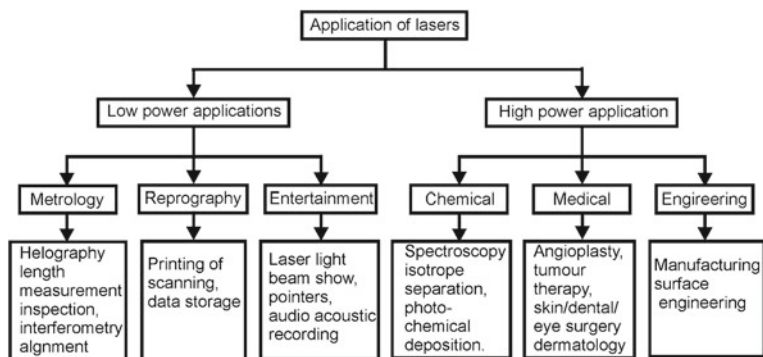


Fig. 1.4 Application spectrum of laser for the benefit of mankind [2]

Accordingly, a host of lasers capable of delivering a wide variety of wavelength, energy, temporal/spectral distribution, and efficiency have been developed over the past several decades [1–3].

1.5 Laser Assisted Fabrication of Engineering Materials

The increasing demand for laser in materials fabrication can be attributed to several unique advantages like fast processing speed, complete automation worthiness, non-contact processing, elimination of subsequent finishing operation, reduced processing or operational cost, improved product quality, greater material utilization, and minimum heat affected zone [1–3]. Figure 1.5 shows a general classification of the laser assisted fabrication techniques. In general, application of laser to materials fabrication can be grouped into two major classes (a) applications requiring limited energy/power and causing limited microstructural changes only within a small volume/area without change of state and (b) applications requiring substantial amount of energy to induce the change in state and phase transformation in large volume/area. The first category includes polymer curing, scribing/marking of integrated circuit substrates, etc. The second type of application encompasses cutting, welding, surface hardening, alloying, and cladding. The average power or energy input is relatively low in the first category, while that for the second category is higher as the processes involve single or multiple phase changes within a very short time. Almost all varieties of lasers can perform both types of operations in continuous wave and pulsed mode provided appropriate power/energy density and interaction time for the given wavelength are applied.

The classification based on state or phase change is too academic to be of practical use to end users. From the application point of view, laser material processing, as earlier stated, can be broadly divided into four major categories, namely, forming (changing shape or producing a component to manufacture a near net shape

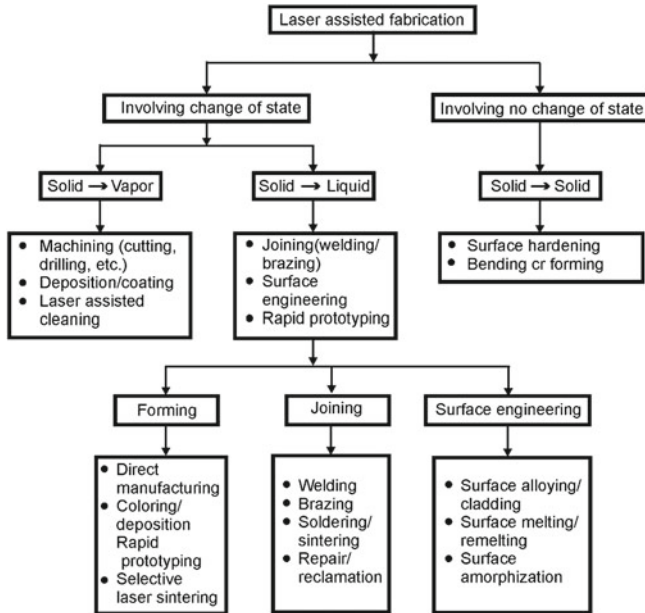


Fig. 1.5 General classification of laser assisted fabrication of materials for engineering applications

or finished product), joining (combining components by fusion welding, brazing, etc.), machining (removing material by cutting, drilling, etc.) and surface engineering (processing confined only to the near-surface region) [2–4]. Figure 1.5 presents this classification with a few representative examples from each category of application. However, this classification is based on the general definition and scope of the processes as understood in conventional practices.

The domain for different laser assisted fabrication techniques as a function of laser power and interaction time is illustrated in Fig. 1.6 [2]. The processes are divided into three major classes, namely involving only heating (without melting/vaporizing), melting (no vaporizing), and vaporizing. It is evident that transformation hardening, bending, and magnetic domain control which rely on surface heating without surface melting require low power density. On the other hand, surface melting, glazing, cladding, welding, and cutting that involve melting require high power density. Similarly, cutting, drilling, and similar machining operations remove material as vapor hence, need delivery of a substantially high power density within a very short interaction/pulse time. Since all laser material processing operations can be defined by an appropriate combination of power density and interaction time, one is tempted to combine these two into a single scalar parameter like energy density (power density multiplied by time, J/mm^2) for the sake of simplification and convenience. However, the exercise is bound to prove futile and not advisable as both the quantum of energy and its temporal and spatial interaction with matter (rather than their product) is crucial to achieve the desired microstructural/phase/state changes and properties for

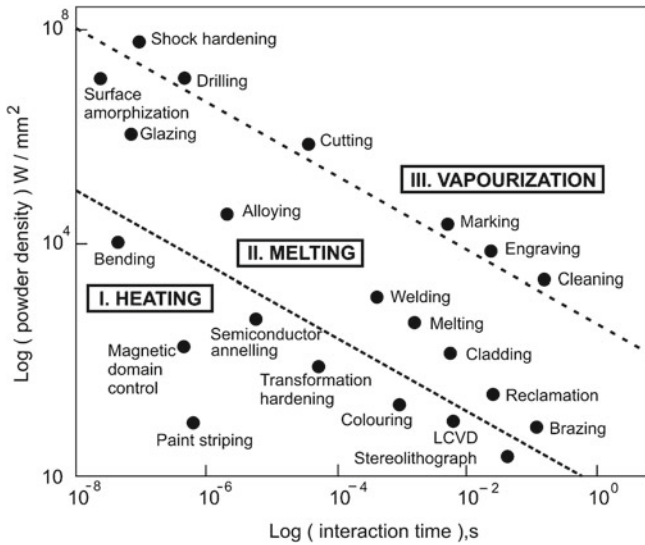


Fig. 1.6 Schematic process map in terms of combination of laser power density and interaction time for different types of laser material processing involving either no (only heating) or change of state (melting or vaporization) [2]

a given material. For instance, application of 10^{-2} J/mm² energy density may induce either surface hardening (say, for a given material combination of 10^2 W/mm² power density and 10^{-4} s interaction time) or surface melting (say, for a combination of 10^4 W/mm² power density and 10^{-6} s interaction time).

In laser assisted fabrication, a high-power laser beam interacts with the workpiece while a high relative speed is maintained between the two. The workpiece is usually mounted on a table capable of translation along two mutually perpendicular directions with a speed precisely controlled by a computer numerical controller. For convenience, the laser beam is kept stationary and the specimen is moved at a high speed. Several laser and material variables, either independent or dependent, play important roles in determining the final properties and characteristics of the processed zone. The independent variables are laser power, beam size, beam configuration, traverse speed of the workpiece, surface roughness, temperature, and surface condition of the substrate. The dependent variables are absorption coefficient, coverage rate, composition, and microstructure of the surface/near-surface region, hardness, residual stresses, heat-affected zone (HAZ) size, physical, mechanical, and electrochemical properties of the workpiece.

Laser power necessary for surface melting of metallic materials is generally high due to high reflectivity and thermal conductivity of metals. Reflectivity of the metal surface is actually related to electrical conductivity. The beam size determines the power density on the specimen surface (power density is defined as the power divided by the cross-sectional area of the laser beam). As already explained, the

combination of laser power density and interaction time should be carefully chosen during processing of materials by laser as this very combination primarily determines the scope and success of the process and properties for a given materials (Fig. 1.6).

Beam configuration or beam profile plays an important role in determining the energy distribution at the interaction zone during laser processing. Four types of beam profiles, namely Gaussian, multimode, square (or rectangular), and top hat are commonly used for material processing [2]. A Gaussian beam is most suitable for cutting and welding applications rather than for surface treatment because, being a ‘sharp tool,’ it tends to vaporize and melt the substrate deeply. In contrast, multimode, top hat, and square profiles (‘blunt tools’) are preferred for surface engineering. These beam profiles offer suitable surface casing with wider coverage rates and uniform case depths. Square and rectangular beam profiles are generated by using an optical integrator or scanner.

In the following sections, we will now review the individual classes of laser material processing and the current status of understanding.

1.6 Laser Assisted Shaping

The high power laser beam may be used as a source of heat to shape components in the desired dimension, shape, geometry, design, and properties. Laser material processing offers a unique possibility of manufacturing finished components directly from the raw materials without any elaborate intermediate operation [1–4, 27]. A one-step fabrication is most attractive, obviously for the tremendous economy in time, cost, material, and manpower associated with it than that necessary in the usual route of fabrication involving several intermediate stages/steps. Shaping of components by laser may be achieved by thermal stress assisted deformation (bending), direct forming of component from powder or wire by rapid prototyping/manufacturing, and reclamation/repairing [1–4]. These processes distinguish themselves from other laser material processing methods in their proclaimed objective of single-step manufacturing of a finished or semi-finished product than contributing toward any other intermediate processing steps like machining, joining, or surface engineering. For brevity, we will address all these laser assisted versions of otherwise conventional manufacturing processes as laser forming. In this section, laser assisted manufacturing techniques like laser bending and direct laser manufacturing techniques will be discussed in detail.

1.6.1 Laser Assisted Bending

Laser assisted bending involves modifying the curvature of sheet metal by thermal residual stresses induced by laser assisted heating without any externally applied mechanical forces [28–34]. Laser assisted bending also serves the purpose of straight-

ening thin sheets by a similar laser-based non-contact process. The process assumes significance due to the ease and flexibility of non-contact processing, amenability to various types of materials and direct manufacturing of components with diverse shape/geometry, properties and composition with high precision/ productivity. Laser assisted bending involves a complex interplay between the thermal profile and stresses generated by laser irradiation, which in turn depend on many parameters such as laser power density, interaction/pulse time, material properties (thermal, physical or chemical), and dimension/geometry of the work piece (thickness, curvature, etc.). Bending of strong and difficult-to-bend metals (body centred cubic, BCC or hexagonal close packed, HCP), intermetallics, composites, and ceramics have been an important motivation for the increasing interest in laser assisted bending. The success of laser bending of semiconductor and polymeric sheets are of great interest to the semiconductor and packaging industry.

There are three mechanisms of laser assisted bending, i.e., temperature gradient mechanism, buckling mechanism, and upsetting mechanism [30–35]. Many applications involve a complex combination of these mechanisms rather than only one of them.

1. Temperature Gradient Mechanism

Temperature gradient mechanism is operative when a steep temperature gradient across the thickness of sheet metal is encountered, particularly when the beam diameter is typically of the order of sheet metal thickness or width and the traverse rate is fast enough to maintain a steep temperature gradient. Figure 1.7a explains the thermal history and mechanism associated with temperature gradient assisted bending of sheet. At the initial stage of laser heating, the surface of the metal facing laser is heated up leading to counter-bending of the sheet away from the laser beam as a result of rapid thermal expansion of the top-surface than the bottom layer. Further heating leads to decreasing the flow stress in the heated area and increasing thermal expansion of the surface layer. At a certain temperature, the geometry and degree of counter-bending reach the maximum elastic strain that the metal can endure beyond which plastic compressive strain sets in with further increase in temperature and thermal expansion. These plastic compressive strains accumulate until laser irradiation shifts to allow cooling to begin mainly due to self-quenching with the heat flowing into the surrounding bulk to cool the irradiated zone within 10–20 s. During cooling, shrinkage of the heated material occurs both due to natural contraction on cooling and plastic compression induced by prior laser heating. Due to the differential lengths between the top and bottom surface layers of the sheet, a bending angle develops toward the laser beam.

2. Buckling mechanism

The buckling mechanism will occur if the beam diameter of laser is large compared to the sheet metal thickness, laser beam intensity profile is Gaussian or multiple Gaussian, and the processing time is low, resulting in a small temperature gradient across the sheet metal thickness. Figure 1.7b describes the principle of laser bending by buckling mechanism. Primarily, the material is heated, which in turn leads to the thermal expansion and generation of compressive stresses in the neighboring heated

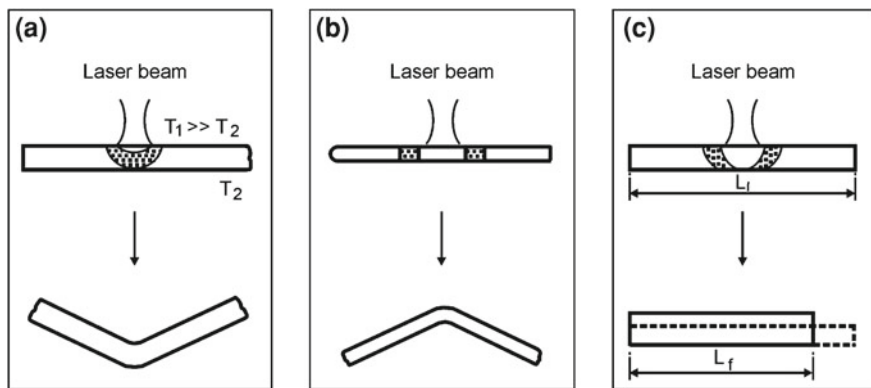


Fig. 1.7 Deformation modes of laser bending based on (a) temperature gradient mechanism, (b) buckling mechanism, and (c) upsetting mechanism, respectively. T_1 and T_2 are temperatures on opposite surfaces. L_i and L_f are the initial and final lengths of the sheet [30]

region. If the heated area is large enough with a small natural deviation from the perfect plane, an instability, or buckle, develops. At the center of the buckle, the temperature is extremely high, therefore the flow stress in this region is relatively low and the bending of the sheet in this region is totally plastic. In contrast, the root (or end) of the buckle, which is far away from the center of the laser beam, is heated to a much lesser extent with smaller temperature rise. If the flow stress is relatively high, this small temperature rise can only result in complete elastic bending. By controlling appropriate parameters, positive (concave bending toward the laser beam) or negative (convex bending away from the laser beam) bending can be achieved with the buckling mechanism [35]. As the beam moves along the surface, the buckle shifts along the bending edge. The relative motion between the beam and work piece along the surface can also alter the stiffness of the work piece. At the start of the buckling process, the bending legs are held in the original plane due to the stiff surrounding material. However, the force that holds the bending legs straight decreases with increase in amount of forming. Therefore, the elastic part of the buckle relaxes and only the plastic part remains in the sheet, resulting in an angular bend. Because the buckling mechanism results in more energy being coupled to the work piece, bending angle often up to 15° is achieved after a single pass.

3. Upsetting Mechanism

The upsetting mechanism occurs if the laser beam diameter is in the order of or less than the sheet metal thickness with a very low traverse speed. The low processing speed will result in almost homogeneous heating across the thickness of the sheet metal. Owing to the temperature increase, the flow stress decreases in the heated area and the thermal stress approaches the elastic limit. Additional heating leads to a plastic compression of the heated material as it is hindered in free expansion by the surrounding bulk material. Therefore, a large amount of thermal expansion is converted into plastic compression. During cooling the material contracts and the

plastic compressive strain remains in the sheet for exactly the same reason as in the temperature gradient mechanism. Owing to the constancy of volume, there is an increase in the sheet thickness in the compressed area. Figure 1.7c shows the process of laser assisted upsetting that leads to shrinkage of initial length, L_i to smaller final length, L_f with a concomitant increase in thickness from the initial dimension (shown by broken lines).

The concept of laser bending may be extended to straightening of a welded component in a car body to reduce distortion arising out of welding [35], and deep drawing [36]. Laser bending may be combined with conventional forming to blend the high speed of conventional forming with the accuracy of laser forming without any special setup [37]. In laser assisted deep drawing, a laser beam is used to heat the wire to a critical temperature in order to make the wire plastic and easily deformable. Wire feeding and pulling rates are maintained through a feeder and puller roller at a predetermined speed to achieve the desired drawing ratio. The process was applied to nickel wire and was reported to exhibit an increased drawability as compared to the conventional technique, though laser parameters were reported to play a role in determining the drawing limit [36]. Brittle materials can also be successfully drawn without any rupture or micro-crack using laser.

The prediction/optimization of laser parameters may be attained by a detailed theoretical model. Deformation behaviors of Ti-based alloys were extensively studied Chen et al. [38] using finite element method. Marya and Edwards [39] analyzed the laser bending of two titanium alloy sheets, Ti-6Al-2Sn-4Zr-2Mo (near-alpha alloy) and Ti-15V-3Al-3Cr-3Sn (beta alloy) using a conduction model with a traveling Gaussian heat source. Temperature and bending angle were predicted and correlated with process parameters. Bending was found to initiate at 0.48 of the melting temperature and attained a maximum value at approximately 0.65 of the melting temperature. The effect of process parameter on bending angle was explained by analytical model developed by Cheng and Lin [40] and also 3-D finite element simulation by Kovacevic et al. [41]. The experimental results were suitably compared with the theoretical prediction. Laser bending of cold rolled steel was studied by Peng and Lawrence [42] where, the effects of the plastic anisotropy on bending deformation during the laser forming process have been investigated both experimentally and numerically. Most of the research articles concern a detailed experimental observation of studying the effect of laser parameters on the bending characteristics of different materials. Studies on AISI 1008 steel and mild steel show that bending angle increases with increase in laser power and number of repetitions, on the other hand, it decreases with increase in scan-speed and beam size/diameter for [43, 44]. The bending angle usually increases with increase in thermal-effect index (coefficient of thermal expansion divided by the product of density and specific heat). However, strength or modulus has no significant influence on it [43]. Among the geometric parameters, sheet thickness influences the bending angle the most, and the latter decreases sharply with increase in sheet thickness [43]. The bending behavior of AISI 304 austenitic stainless steel wire (0.1 mm diameter) to develop complex frame structures such as zigzag or crank wire frames was studied by Yoshika et al. [45] with a Nd:YAG laser offering 0.02 – 0.2 J energy. Besides fabricating to the desired complex shape, it

also improved the strength of the frame structure. The investigation on laser bending of AISI 304 stainless steel of different thicknesses using continuous wave CO₂ laser showed that the rate of bending increased with increase in applied power density and the effect was more significant at a higher number of passes. However, an optimum range of laser power should be selected so that the applied power density is capable of bending without excess melting, evaporation, or crater formation. The rate of bending increased with increase in the number of passes due to increase in cumulative thermal stress. The thermal stress generated in each pass was proportional to the thermal gradient. Furthermore, cross-sectional thickness at the bent region is progressively reduced during successive passes due to material flow away from the bent region after each pass. Microstructural analysis of different regions of the bent surface and its variation with laser parameters were undertaken to understand the mechanism of bending. Figure 1.8a–c show the microstructure of the (a) irradiated region, i.e. inner side of bending, (b) solid-liquid interface and (c) heat affected zone of the irradiated zone, of laser bent AISI 304 stainless steel lased with a power density of $19.6 \times 10^7 \text{ W/m}^2$, scan speed of 4 m/min and 10 passes. Figure 1.8a suggests that laser irradiation causes melting and high rate of quenching of the near-surface region to develop a very fine-grained and equiaxed microstructure at the near-surface region. Refinement of microstructure achieved in laser bending operation is beneficial in increasing the strength without sacrificing the ductility of the inner side of the laser bent zone. Although melting occurs at the irradiated region, subsequent rapid solidification leads to formation of a defect-free and continuous remelted region or interface (Fig. 1.8b). It is apparent that fine dendrites form and grow from the former solid-liquid interface. Microstructure in the narrow heat effected zone shows evidences of grain coarsening due to heat flow beyond the thin surface wetted region (Fig. 1.8c) [46]. A detailed XRD analysis of the bent zone revealed that, while phase aggregate remained the same, lattice strain due to thermal effect led to measurable broadening of peaks [46].

Besides microstructure, laser bending affects microhardness in different zones depending on the laser parameters adopted. Figure 1.9 shows the variation of microhardness with distance at different regions of laser bent steel (lased with a power of $54.3 \times 10^7 \text{ W/m}^2$, scan speed of 5,000 mm/min). Microhardness increases to 250 VHN as compared to 190 VHN of the substrate at the inner bent zone. The microhardness further increases after multiple passes (275 VHN after 40 passes) possibly due to recrystallization and grain refinement effect. The sudden rise in hardness immediately after the melt zone is attributed to the formation of Cr₂₃C₆ precipitates along the zone near to the solid-liquid interface [46].

Subsequent grain coarsening in the heat affected zone reduces the hardness considerably resulting in a sudden drop in microhardness (Fig. 1.9). On the other hand, microhardness of the outer bent zone (reverse side of the irradiated zone) is marginally increased due to working effect (as also evident from Fig. 1.9). The microhardness of melt zone and outer zone along the centerline of the bent sheet is, however, found to vary with laser parameters. Increase in the number of passes increases the microhardness of the irradiated zone due to microstructural refinement [46]. On the other hand, the hardness of the outer bent region increases with increased number of passes

Fig.1.8 Scanning electron micrographs of the (a) irradiated region, i.e., inner side of bending, (b) solid–liquid interface, and (c) heat affected of laser bent AISI 304 stainless steel irradiated with a power density of $19.6 \times 10^7 \text{ W/m}^2$, scan speed of 4,000 mm/min and 10 number of passes [46]

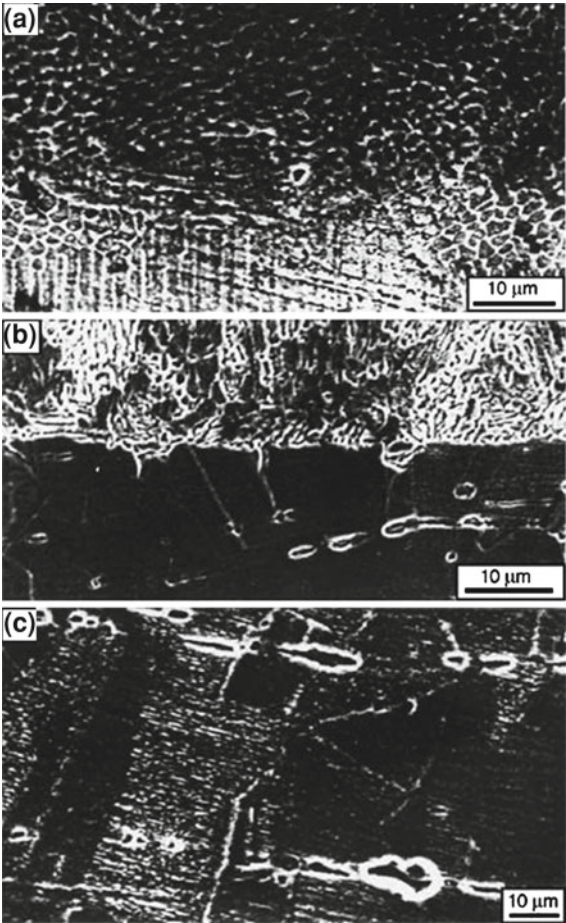
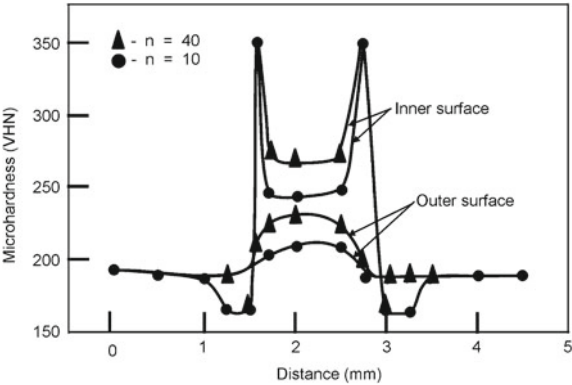


Fig.1.9 Distribution of microhardness along the length of laser bent AISI 304 stainless steel (sheet thickness of 0.9 mm, lased with a power of $54.3 \times 10^7 \text{ W/cm}^2$, scan speed of 5,000 mm/min) [46]



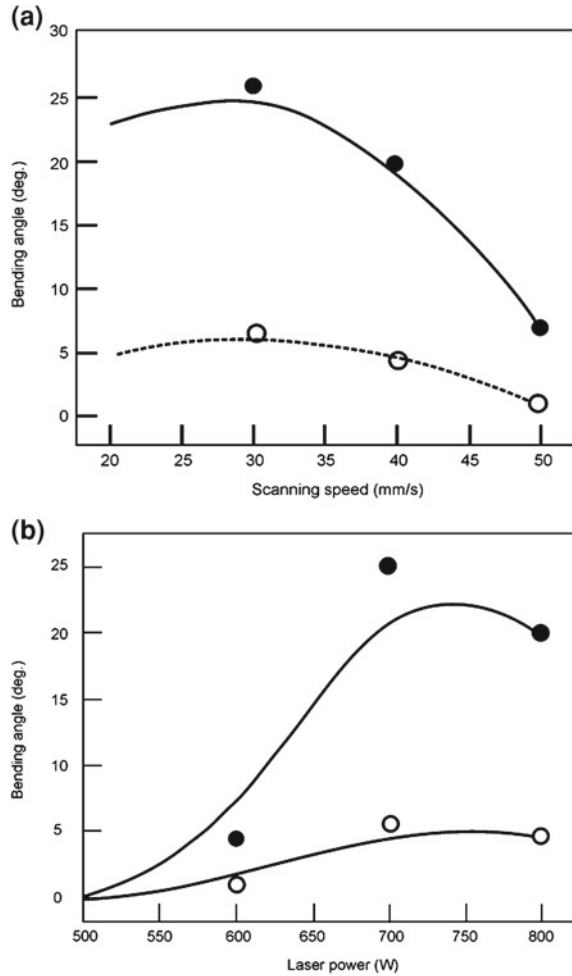
mainly because of a larger degree of deformation induced at greater thermal stress developed due to repeated irradiation. Hence, laser bending is a unique technique of bending of sheet metals with an improved mechanical property at the centerline of laser bending.

In case of materials which undergo phase transformation, the phase transformation stress should also be taken into account. Wang et al. [47] studied the bending of St C45 steel (C: 0.08, Si: 0.3–0.1, Mn: < 0.4, P : < 0.025, S : < 0.025) by a continuous wave CO₂ laser and observed that the final deformation angle was found to depend on a combined action of thermal strain and phase transformation strain. Bending of tube is primarily achieved through thickening of the scanned region instead of thinning of the un-scanned region, and the scanned region assumes a slightly protruded shape [48]. The importance of the process lies on bending of metal matrix composite and difficult to bend materials. Laser assisted bending has been studied in Ti and its alloys [49–56]. Magee et al. [50–52] studied the influence of process variables on laser bending of $\alpha + \beta$ Ti alloy (Ti–6Al–4V) using a continuous wave CO₂ laser. Blake et al. [53, 54] studied the effect of beam divergence, feed rate, laser power, and pulse width on the angle and range in laser assisted bending of Ti–6Al–4V and Ti–15V–3Cr–3Sn–3Al using a 400-W pulsed Nd-YAG and 50 W desktop CO₂ laser. Similarly, Maher et al. [55] and Hatayama and Osawa [56] investigated the effect of process variables on the bending behavior of pure Ti. Marya and Edwards [39] studied the interactions between process variables, materials properties, and residual angular distortions (bending angle) during laser assisted bending of Ti–6Al–2Sn–4Zr–2Mo and Ti–15V–3Al–3Cr–3Sn alloys.

Okuda et al. [57] studied the deformation mechanism of Mg alloy by finite element modeling. Chan et al. [58] compared the deformation behavior of chromium sheet having limited room temperature ductility subjected to roll compression and laser bending technique. In roll compression test, a bending angle of 90° was achieved without fracture at a temperature of 100°C. However, the maximum bending angle achieved by non-contact laser bending was 23.5° and the same was found to increase with increase in applied power density and number of irradiation.

The deformation behavior of SiCp reinforced 6,092 aluminum matrix composite using a 2 kW Nd:YAG laser was studied by Liu et al. [59]. Figure 1.10 shows the variation of bending angle as a function of (a) laser scanning velocity at laser powers of 500 W and (b) applied power at an average scan speed of 5 mm/s. It is evident that the bending angle decreases with increase in scan speed because of the decrease in interaction time between the laser beam and composite. On the other hand, the bending angle increases with increase in applied power. However, when the applied power is above 700 W, there is no more increase in the bending angle. Under a suitable condition for bending, a linear relationship between the bending angle and the number of irradiation passes was observed. Ramos et al. [60] investigated the microstructures of Alclad 2024–T3 Al–Cu alloy following bending by a CO₂ laser. It was observed that the irradiated zone experienced different stages of thermal annealing including recovery (sub-grain formation), recrystallization, and grain growth depending on the deposited thermal energy. Recrystallized zone suffered partial melting at the grain

Fig.1.10 Variation of bending angle as a function of (a) scanning speed at an applied power of 800 W, and (b) applied power at a scan speed of 40 mm/min for laser bent SiC dispersed 6092Al matrix composite lased with a continuous wave Nd:YAG laser [59]



boundary corners or triple points leading to precipitation along grain boundaries on cooling.

In spite of its poor room temperature ductility, Ti_3 Al-based intermetallic alloy was reported to be laser bent by Yet Chan and Liang [49] primarily due to the differential degree of thermal expansion of the intermetallic across the thickness. A linear relationship between laser bending angle and line energy was observed when the line energy was between 1 and 5 J/mm². Significant changes in microstructures were observed in the alloy after bending without formation of cracks or voids. The hardness profile and microstructure of the deformed specimen revealed that there was a steep temperature gradient across the thickness and the laser bending mechanism was related to that gradient.

1.6.2 Laser Rapid Prototyping

One of the most recent applications of laser in material processing is the development of small, complex, and intricate components by coupling laser with computer controlled positioning stages and computer-aided engineering design [61–66]. This technology is based on repetitive deposition and processing of material layers known as additive freeform fabrication technique [67, 68]. The advantages offered by these techniques include the capabilities to produce components of intricate shape with a greater accuracy, faster processing speed, economy in energy and material consumption, etc. Over 40 different types of additive free-forming technologies have been identified for component development with size ranging from desktop unit to machine tools [69, 70]. In all cases, these technologies are capable of manufacturing parts/components in a single step without the use of specialized tooling, thereby reducing the time needed to manufacture components. Each of these technologies employs the use of computer-aided design and modeling to directly deliver energy or deposit materials in selective layers during fabrication. Depending on the process, a post processing activity may be needed ranging from powder sintering photopolymer curing or excess material removal to produce the final component. Powder-based additive free forming techniques use powders as raw material in shaping material. In ultraviolet selected laser sintering, a thin layer of photo-curable suspensions of ceramic powders is cured by an ultraviolet laser in selected areas [71, 72]. The extrusion free forming technique uses temperature sensitive monomers or reactive compounds in aqueous ceramic slurry to fabricate solid, “gelled” ceramic bodies [73].

On the other hand, the laminated tape method uses ceramic green tapes prepared from evaporation casting of non-aqueous slurries to fabricate parts with a laser-cut, stack, and laminate sequence similar to the laminated object manufacturing process [74, 75]. With this technique, complex high density silicon nitride components with internal passages have been developed for potential use in rocket engine injectors [76].

Ceramic three dimensional printing methods involve the use of an ink-jet mechanism to inject organic binder into a ceramic powder substrate. Freeform powder melding is a more recent development which uses deposition of sinterable part powders and unsinterable tool powder in selected areas of each layer to build a three-dimensional part. In stereolithography, the solid object is made by scanning an ultraviolet laser beam over the surface of a bath of epoxy resin that hardens on exposure to the ultraviolet light. Once a layer is complete, the base plate moves down a little in the bath and a new layer of liquid flows in over the top to enable the next layer to form on top. The layer building continues until the component is ready in the desired dimension [77]. In selective laser sintering, instead of liquid resin, a fluidized powder bed or sheet is used that is heated close to its melting point. The carbon dioxide laser beam scans over the powder and heats the grains so that they undergo incipient melting and sintering. Subsequently, the base plate moves down

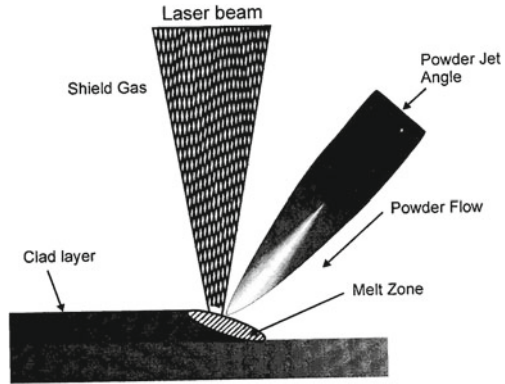
slightly, and the next layer of powder is spread across the surface by a rotating roller [77]. The process continues until the desired shape or object is ready.

In laminated object manufacturing, the pre-form is built from the layers by pulling long and thin sheets of pre-glued paper/plastic across the base plate and fixing it in place with a heated roller that activates the glue [74]. A computer controlled laser head scans the surface and cuts out the outline of the desired object. As the base plate moves down, the whole process starts again. At the end of the build process, the little cross-hatched columns are broken away to free the object. In the fused deposition process, the object is made by squeezing a continuous thread of the material through a narrow nozzle (heated by laser) that is moved over the base plate [74]. As the thread passes through the nozzle, it melts only to harden again immediately as it touches (and sticks to) the layer below. For certain shapes, a support structure is needed, and this is provided by a second nozzle squeezing out a similar thread, usually of a different color to make separating the two easier. At the end of the build process, the support structure is broken away and discarded freeing the object/model. The models made from wax or plastics in this method are physically robust. This new fabrication concept allows construction of complex parts, starting from a three-dimensional computer-aided design model without a mold.

Laser assisted direct metal deposition refers to the additive layered manufacturing technology for building components from a computer-aided design model [2]. Metal powders, injected into the laser focal zone, are melted and then re-solidified into fully dense metal in the wake of the moving molten pool created by the laser beam. Successive layers are then stacked to produce the entire component volume of fused metal representing the desired model. These processes have been proven suitable for fabricating components from nearly any metal system to near net shape accuracy with mechanical properties approaching and in some cases exceeding the properties found in conventionally processed wrought structures.

Figure 1.11 shows the schematic of direct laser fabrication process. Single-step processing by laser engineered net shaping and direct laser fabrication produce cost saving realized by elimination of conventional multi-step thermomechanical processing. Design features such as internal cavities or overhanging features can be made without joined assemblies. Hard to process materials such as intermetallics, refractory metals, and high temperature alloys can be processed in a single step. Functionally graded compositions can be created within three-dimensional components to vary the properties to match localized requirements due to service environment. The technology offers the designer a rapid prototyping capability at the push of a button, without the need to fabricate dies or use of forming equipment or extensive machining and joining processes to produce a part. Future development is still required for these processes to be commercially accepted and used in the industry. Parts are deposited with a surface roughness of 10 μm , arithmetic average, making a secondary finishing operation necessary for some applications to achieve high accuracy and polished surface texture. Residual stress measurement and control is also required to avoid distortion of the deposited components. Motion path and control code needs to be optimized to reduce the overall process time from the computer-aided model to the

Fig.1.11 Schematic of laser deposition process. Powder is carried and delivered by argon gas through the nozzle into the laser beam and the molten metal deposits on the substrate underneath



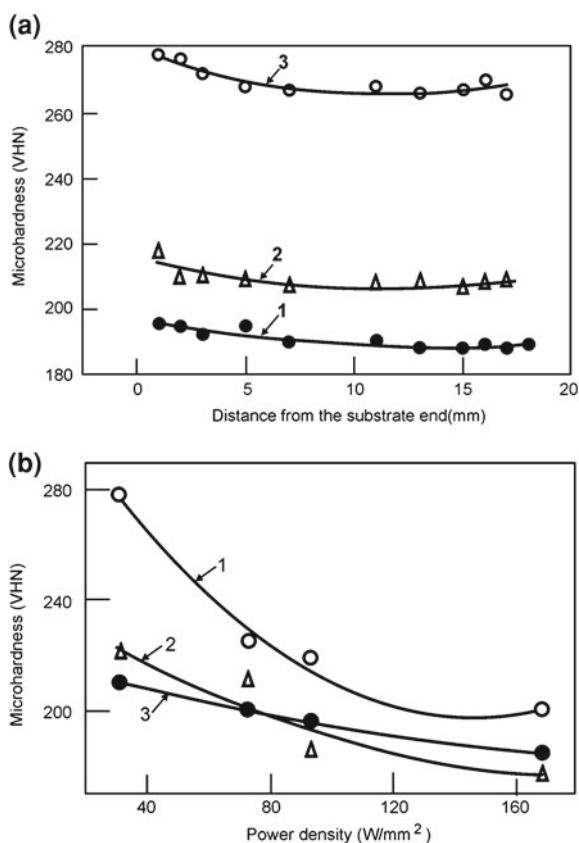
finished part. Lewis and Schlienger [78] have explained the process and its possibility of application in detail.

Laser engineered net shaping is a process in which near-net-shape metal structures are built from powdered metal layer by layer from computer-generated designs. Zhang et al. [79] discussed the characteristics of laser engineered net shaping, directed light fabrication, and shape deposition manufacturing. The fundamental of selective laser sintering has been studied by Goode [80]. Dai and Shaw [81] developed a 3-D thermomechanical finite element model to investigate the transient temperature and residual stress fields in laser assisted fabricated part. The model system chosen was 93Cu+7Sn and NiMo mixed with 70% (MoW)2NiB2:30%NiMo. McAlea et al. [82] discussed the laser-based rapid prototyping technique and compared with the sand and investment casting technique. The possibility of application of laser assisted deposition in fabrication of part in the packaging industry and microelectronic component have been discussed by Bauer et al. [83] and Micheli and Boyd [84], respectively. Griffith et al. [85] described the use of contact and imaging techniques to monitor the thermal signature during laser engineered net shaping. The understanding of solidification behavior, residual stress, and microstructural evolution with respect to thermal behavior were discussed.

Metal rapid prototypes and fabrication of molds using hybrid processes of selective laser cladding and milling techniques have been studied by Jeng and Lin [86]. The injection molding machine used in this study was a metal powder injector with precise temperature control. The chemical composition of the metal powder used in the injection machine was W (93%), Ni (4.9%), and Fe (2.1%). The density of the alloy was 7.9 Mg/m³. The selective cladding process was employed to build up the material layer-by-layer, and the milling operation was employed to level the top surface of the clad to increase the accumulation of powder and accurately control the clad height. Similarly, fabrication of a 3-D structure using micro-electro-discharge machining and laser assembly and application of laser welding of wire, subsequent deposition, and milling for rapid prototyping were discussed by Kuo et al. [87] and Choi et al. [88], respectively. Direct laser sintering of iron, Cr-V tool steel,

7Fe–4.3C, 97Al–3Fe, 93.3Cu–2.8Sn–3.9C and 93.4Fe–1.6C–2.5Cu2.5MoS2 alloys were undertaken and the effect of process parameters on sintering behavior was studied [89]. Tang et al. [90] and Wang et al. [91] carried out selected laser sintering of Cu-based alloys. Khaing et al. [92] developed a 3-D soft and porous structure from a mixture of Ni, bronze and Cu powders using EOS INT M250 laser sintering machine. Kathuria [93] investigated selected laser sintering of 3 dimensional components made of Co, Ni, and Cu alloys. Hayano [94] and Tolochko et al. [95] fabricated dental root implants made of Ti by selected laser sintering. Components of different shapes from AISI 304 stainless steel were fabricated by Jeng et al. [96] using selective laser cladding technique using a Rofin Sinar RS820 1500 W CO₂ laser. The effect of process parameters on the clad height and surface quality has been studied for direct laser deposited AISI 316L stainless steel using diode laser and continuous wave CO₂ lasers [97, 98]. Dutta Majumdar et al. [99, 100] observed that the morphology and degree of fineness of the microstructure of AISI 316L components fabricated using a 1.5 kW continuous wave diode laser were directly related to the laser parameters. The range of grain size (maximum to minimum) was taken as a measure of homogeneity. It was found that the range of grain size and micro-porosity reduced to a minimum with increase in scan speed. Figure 1.12a shows the variation of average microhardness of direct-laser clad AISI 316L stainless steel along the wall growth direction for laser assisted fabricated AISI 316L stainless steel processed with the respective power density and scan speed combinations of (1) 0.091 kW/mm², 2.5 mm/s; (2) 0.091 kW/mm², 5 mm/s; (3) 0.031 kW/mm², 5 mm/s (with a common powder feed rate of 136 mg/s). Figure 1.12b reveals a similar analysis of variation of microhardness with applied power density obtained by laser fabrication with identical conditions of laser cladding. From Fig. 1.12a, it is evident that the microhardness is uniform throughout the cross section along the wall height with a marginally higher value near the substrate and a lower value at the intermediate region. The marginally higher value of microhardness near the substrate region is mainly because of refinement of microstructure due to a high quenching rate from the underlying substrate. On the other hand, lower level of microhardness at the intermediate region is attributed to the grain coarsening effect. Application of a lower power density (plot 3 vis-à-vis plot 2) increases the average microhardness. Similarly, application of a lower scan speed (plot 1 vis-à-vis plot 2), increases the average microhardness of the fabricated layer. Hence, the microhardness of the fabricated layer marginally varies with the position and is highly dependent on the applied laser parameters. Figure 1.12b further suggests that average microhardness of the fabricated layers decreases with increase in applied power density. This effect is attributed to coarsening of grains revealed from a detailed microstructural investigation [99]. A close comparison of plot 1 with plot 2 shows that average microhardness value increases with increase in scan speed. With increasing the scan speed, due to a shorter time of interaction a low energy is supplied during melting resulting in refinement of grains, and hence, increase in average microhardness. The effect of powder flow rate on the microhardness does not however, show any specific trend (plot 2 vis-à-vis plot 3). From the variation of microhardness with laser parameters, it may be concluded that hardening of the formed parts is mainly because of grain refinement

Fig.1.12 Variation of average microhardness with (a) distance or length and (b) applied power density for laser fabricated AISI 316L stainless steel using different combinations of power density, scan speed and feed rate (marked as 1, 2, 3) [100]



and for an improved microhardness, a combination of low power and high scan speed should be chosen. Furthermore, the critical potential for pit formation (E_{PP1}) (550 mV(SCE)) was superior to that of the conventionally processed AISI 316L stainless steel substrate (445 mV(SCE)) also due to pronounced uniformity and refinement of grain size.

Metallic foam is increasingly becoming popular due to its unique combinations of low density and high compressive strength [101]. Aluminum foam has evoked a special interest due to its lightweight structure and possibilities of various structural applications in automotive, aerospace and allied industries. However, manufacturing techniques associated with aluminum foam limits the application of it on a wider scale. Kathuria [102] attempted to fabricate Al-7% Si foam using Nd-YAG laser and obtained a localized and unidirectional expansion of the foam in the direction of laser irradiation with as high as 60% porosity and closed-cell structure. The synthesis involved mixing the alloy powder with a foaming agent, cold isostatic pressing of the mixture to form a foamable sandwich precursor, and heating it up to its melting point by a high power laser beam. Laser irradiation is useful in inducing rapid

decomposition of the foaming agent into hydrogen or some other gaseous product and allowing precipitation of intermetallic phases to strengthen the matrix phase. Zhang et al. [103], Mei et al. [104], Arcella and Froes [105] and Abbott and Arcella [106] attempted fabrication of fully dense and rapidly solidified components by direct laser deposition. Srivastava et al. [107, 108] developed TiAl alloy by direct laser fabrication using gas atomized Ti₄₈Al₁₂Mn₂Nb powder as feedstock and a VFA 600 W CO₂ laser unit. The microstructure was heterogeneous and extremely fine compared to the conventionally processed material. A post heat treatment was found to improve the microstructural and compositional homogeneity. Banerjee et al. [109–111] developed Ti–6Al–4V–TiB, Ti–25%V and Ti–TiB composites using laser engineered net-shaping process. Tomochika et al. [112] attempted to synthesize NiTi intermetallic compound by laser assisted melting of a combination of pure Ti (300 μ m diameter) and pure Ni wire (250/350 μ m diameters) followed by high pressure Ar gas assisted atomization and coating on aluminum substrate. The particle size of the atomized powder ranged from 10 to 125 μ m and the thickness of the coating was 3 mm. The sintered compact of equi-atomic blend of Ti and Ni was single phase NiTi martensite with martensitic (M_f) and austenitic finish (A_f) temperatures of 320 K and 365 K, respectively. Zhang et al. [113] developed TiAl intermetallics by laser engineered net shaping using a continuous wave Nd:YAG laser. Wu and Mai [114] developed Ti and TiAl alloy parts with various geometries by direct laser fabrication. Tang et al. [115] prepared Ti/TiN in situ composites by laser induced reaction between Ti powder and N₂ gas and evaluated their mechanical properties. For complex alloy systems, the microstructure of the direct laser clad component was found to be different from the single clad layer and varied with the numbers of passes.

Karlsen et al. [116] developed the Co-Cr-Mo superalloy for bio-implants with improved biocompatibility. Ni- and Co-based superalloys were fabricated by the direct laser metal deposition technique [116–118]. The tensile strength of the laser consolidated Co-based superalloy was reported to be 50% higher than that of as-cast or powder fabricated components attributed to the exceptionally fine columnar dendrite microstructure produced by the rapid solidification [117].

A new rapid prototyping method has been developed by combining selective laser sintering and gel-casting technique for the fabrication of complex-shaped Al₂O₃ ceramic parts [119]. The process involves aqueous gelcasting to form high mechanical strength Al₂O₃-based green body by in situ polymerization of Al₂O₃ slurry containing monomer and cross-linker, and sintering of the green compact by selective laser sintering machine. The main advantages of the method lie in the absence of any container or die, minimum contamination, and possibility of having high liquid temperatures. Furthermore, the process allows solidification to proceed with a planar and stable liquid–solid interface accompanied by high thermal gradient and high crystal growth rates.

Larrea et al. [120] described the procedure for preparing large surfaces of eutectic composites of Al₂O₃ – ZrO₂, with thickness up to 250 mm, using a modified laser zone melting. The surface of a ceramic precursor is scanned with a rectangular CO₂ laser beam of 20 \times 0.5 mm size which induces surface melting. The microstructure

consisted of fine, alternating, and interpenetrating Al_2O_3 and ZrO_2 single crystal lamellae.

Laser can be a useful tool for in situ rapid fabrication of composite components like cutting tools, shear blades, etc. Lu et al. [121] fabricated TiC dispersed Cu–Ti–C and Cu–Ni–Ti–C composites by laser scanning (using a CO_2 laser) of ball milled powder mixtures of Cu–Ti–C and Cu–Ni–Ti–C. Liu and Du Pont [122] developed crack-free functionally graded TiC/Ti composite materials by laser engineered net shaping with compositions changing from pure Ti to approximately 95 vol% TiC. Kathuria [123] fabricated porous components of 93 % Cu+7 % Sn and 70% (MoW) $_2$ NiB $_2$:30% NiMo alloy powders using Nd:YAG laser. Wang et al. [124] fabricated W/ $\text{W}_2\text{Ni}_3\text{Si}$ ternary in situ metal silicide matrix composites using direct laser deposition. Duan and Wang [125] developed rapidly solidified Cr_3Si metal silicide ‘in situ’ composites by laser melting of Cr–Si–Ni alloy powders. Cheng et al. [126] studied the influence of process parameters on structure and integrity of Al/SiC composite by direct laser deposition.

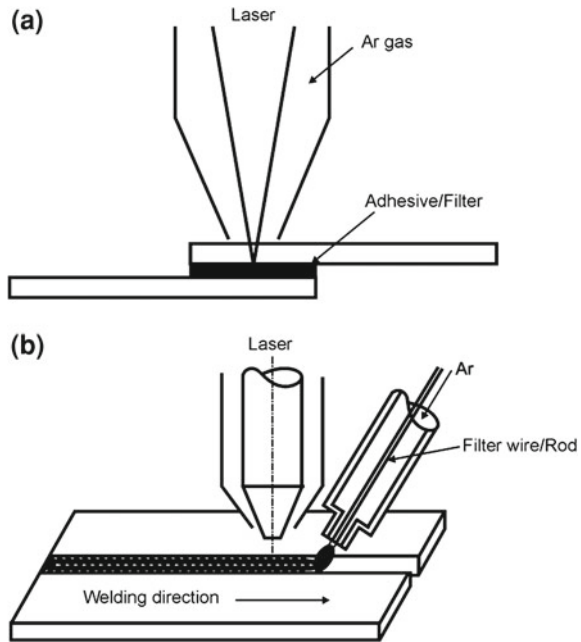
An intelligent laser processing based on size-dependent optical absorption coefficient of metal particles has enabled fabrication of almost mono-dispersed metallic nanoparticles on a chosen substrate [127]. Using this method, Ag clusters with mean diameters of 10 nm and size distributions of 0.13 have been prepared [127].

Irradiation with the second harmonic generation of 1.06 μm Q-switched Nd:YAG laser on powdered nonlinear crystals suspended in a photopolymeric solution enabled high resolution rapid prototyping [65]. One such structure developed by this method was a 3-D periodic photonic band-gap structure of aluminum oxide that consisted of layers of parallel rods forming a face-centered tetragonal lattice [128]. A similar laser-driven direct-write deposition technique (from trimethylaminealane and oxygen precursors) was successfully utilized to fabricate a 3-D microstructure consisting of aluminum oxide and aluminum [129]. These laser deposited rapid prototype ceramic components are useful as micromechanical actuators like microtweezers and micro-motors.

1.7 Laser Joining

Joining of similar or dissimilar materials may be achieved by using high power laser beam as a source of heat. Laser assisted joining offers the following advantages over conventional fusion or arc welding processes: high welding speed, narrow heat affected zone (HAZ), low distortion, ease of automation, ability for single-pass joining of thick sections, and better design flexibility with controlled bead size [2, 77]. Laser assisted joining may include welding, brazing, soldering, and micro welding. However, as joining of materials requires a laser source capable of delivering high power density, pulsed or continuous wave Nd:YAG, CO_2 laser and diode lasers are commonly used for joining. Laser assisted joining is applicable to both inorganic/organic and similar/dissimilar materials with an extremely high precision, versatility, and productivity that can only be matched by electron beam welding.

Fig. 1.13 Schematic views of laser assisted (a) lap welding, and (b) butt welding

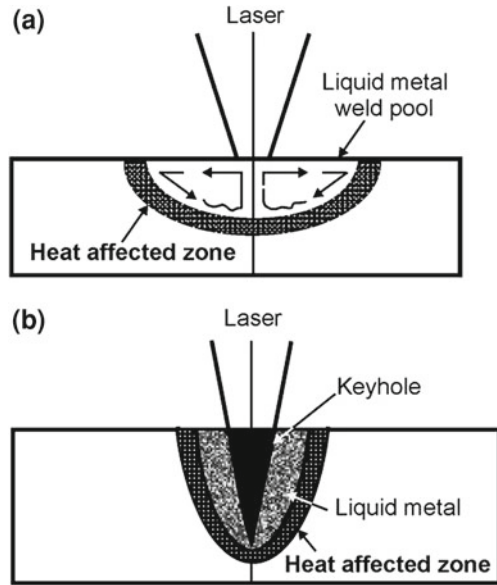


Moreover, laser assisted joining can be done in atmosphere (with proper shrouding), unlike the vacuum processing needed in electron beam welding.

Laser welding is the emerging and most important operation among the laser joining processes [2, 130–154]. Figure 1.13a, b show the schematic set up for laser welding with (a) lap welding and (b) butt welding configuration. The focused laser beam is made to irradiate the work piece or joint at the given location with a finite beam size, configuration and speed. A shroud gas at adequate flow rate protects the weld pool from undue oxidation. Laser heating partially melts and fuses the work pieces or plate edges and joins the adjoining surfaces once solidified after the beam is withdrawn. In case of welding with filler, melting is primarily confined to the feeding wire tip while a part of the substrate being irradiated melts to ensure a smooth joint. In either case, the work piece rather than the beam travels (say, along y in Fig. 1.13a and along x in Fig. 1.13b) at a rate conducive for welding with a minimum heat affected zone.

There are two fundamental modes of laser welding depending on the beam power/configuration and its focus with respect to the work piece: (a) conduction welding and (b) keyhole or penetration welding (Fig. 1.14a, b). Conduction welding occurs when the beam is out of focus (above the surface) and power density is low / insufficient to cause boiling at the given welding speed. In deep penetration or keyhole welding, the beam focus lies below the surface so that sufficient energy per unit area is available to cause evaporation and formation of a hole in the melt pool. The ‘keyhole’ behaves like an optical black body in that the radiation enters the hole and

Fig. 1.14 Schematic of **a** conduction melt pool (*semi-circular*), **b** deep penetration (*key hole*) fusion zone and weld [178]



is subjected to multiple reflections before being able to escape. The transition from conduction mode to deep penetration mode occurs with increase in laser intensity and duration of laser pulse applied to the work piece.

The welding efficiency can be expressed in terms of the power (or energy) transfer coefficient (η) where η is the ratio between laser power absorbed by the work piece and incident laser power. η is usually very small but can approach unity once a keyhole has been established. The melting efficiency or melting ratio (ε) is given by,

$$\varepsilon = \frac{v d W \Delta H_m}{P} \quad (1.7)$$

where, ε is the rate of melting, P the incident laser power, v the welding speed, d the sheet thickness, W the beam width, and ΔH_m the enthalpy or heat content of the metal at the melting temperature. The maximum value of ε is 0.48 for penetration welds and 0.37 for conduction welds [135].

Laser assisted welding has been successfully implemented in a large number of metallic materials [138, 155–178]. High speed laser welding of tin plate and tin free steel for container industries was reported by Majumdar and Steen [158]. Yang and Lee [159] measured the low cycle fatigue strength and residual stress of laser spot welded mild steel (using a continuous wave CO₂ laser) and compared the weld strength with that welded by resistance spot welding. Finite element modeling revealed that residual tensile stress was distributed over the inner and outer rims of the fusion zone. Banas [160] conducted high power laser welding experiments with austenitic stainless steel and showed an equivalent strength in the weld joint as

compared to that of the base metal. Shielding gas was also found to play a major role in determining the quality of the weld zone [161]. It was observed that shielding gas determines the period, size and shape of the plasma created by laser irradiation depending on the ionization potential, dissociation potential, thermal conductivity, and atomic weight of shielding gas. Ghaini et al. [162] studied the influence of laser pulse energy, duration, and travel speed on weld dimension, microstructure, and hardness during overlapping laser assisted bead-on-plate spot welding of low carbon steel using a pulsed Nd:YAG laser.

Kwok et al. [163] fabricated austenitic (S30400 and S31603), duplex (S31803) and super duplex (S32760) stainless steels by laser penetration welding with a continuous wave Nd:YAG laser in an argon atmosphere. The welds exhibited passivity but their pitting corrosion resistance deteriorated as compared with that of the unwelded specimens which is attributed to micro-segregation in the weld zone of S31603, and to the presence of δ -ferrite in S30400, and the change of the ferrite/austenite phase balance in duplex grades S31803 and S32760 in the weld zone.

Laser parameters also play a role in determining the optimum quality of the weld zone. Depending on the base metal thickness, parameters like laser power, welding speed, defocusing distance, and shielding gas should be carefully selected so that weld joints having complete penetration, minimum fusion zone size, and acceptable weld profile are produced [140]. Chan et al. [165] carried out welding of 0.5, 0.6, 0.8, and 1.0 mm thick steel sheets to form tailored weld blanks with different thickness ratios of 2 (0.5/1.0 mm), 1.67 (0.6/1.0 mm), and 1.25 (0.8/1.0 mm) using an Nd:YAG laser. The forming limit diagrams of the tailor-welded blanks indicated that the higher the thickness ratio, the lower the formability of the tailored weld blanks [165]. Costa et al. [167] studied the weldability of hard metal (K40, 88% WC, 12% Co, and K10, 94.4% WC, 5.6% Co) to steel with a high power continuous wave CO₂ laser or Nd:YAG laser and pulsed Nd:YAG laser. Weld bead size, microstructure, bending strength, and hardness were evaluated to correlate the mechanical properties with the concerned welding parameters to obtain full penetration and high strength joints. K40 (88% WC, 12% Co) quality tips have higher resistance after welding, compared to that in K10 samples, that contained cracks after welding. It was concluded that laser welding particularly with continuous wave Nd:YAG laser was an effective joining technique for hard metals, vis-à-vis brazing or mechanical clamping, for manufacturing cutting tools with small weld beads and heat affected zone and a minimum residual stress.

Electro-galvanized steel sheet with zinc coating (thickness of 7.5 μm) was laser welded using a continuous wave CO₂ laser with 23 mm beam diameter having near Gaussian beam configuration. Subsequent electrochemical tests in 1 N NaCl solution revealed the presence of Zn–Fe intermetallic phases in the heat affected zone that accounted for improved adhesion and better sacrificial protection against corrosion [168]. Iqbal et al. [169] developed a new method of using two tandem laser beams for lap welding of galvanized steel sheets. This involves a pre-cursor beam and a higher power actual beam, generated independently or otherwise split from the same source. The first beam cuts a slot, thus making an exit path for the zinc vapors, while the second beam performs the desired welding. The process is easier as it does not need any preprocessing, prearranging with additional components or contour limitations

and the welders may proceed with the jobs as per non-coated steel and applying the technique, the weld zone can get rid of all or a part of the zinc vapour porosity at lower or higher speed, respectively. The experimental results seem promising showing the total absence of zinc in the welds. However, selection of proper source, beam alignment (between weld and cut), and proper sheet clamping are important.

Laser welding of lightweight metals like Al, Mg, Ti, and their alloys for aerospace applications have been reviewed by Schubart et al. [179]. Both conduction-mode and keyhole-mode welding are possible in aluminum [138]. Weld pool shapes in aluminum depend on the mean power density of the laser beam and the laser pulse or interaction time. Transition from conduction- to keyhole-mode welding is known to occur in aluminum at a power density of about 10 GW/m^2 , compared to about 4 GW/m^2 for stainless steel. In both materials, large occluded vapor pores near the root of keyhole-mode welds are common at higher power density due to hydrogen. This porosity problem can be reasonably eliminated by surface milling and vacuum annealing [138].

In comparison with electron beam welding, laser welding yielded a higher fusion-zone depth to width ratio, cooling rate and porosity, and a lower solute loss and post-weld tensile strain [139]. A similar investigation on microstructural evaluation following autogenous bead-on-plate CO_2 laser welding of an Al-8.5Fe-1.2V-1.7Si alloy (in wt. %) on 2 mm thick sheet showed that the fusion zone microstructure consisted of faceted precipitates of around $10 \mu\text{m}$ embedded in cellular-dendritic α -Al matrix with submicrometer intercellular phases [180]. Continuous wave Nd:YAG laser welding of AA5083-O wrought aluminium alloy with a high Mg content (4.5%) and A356 cast aluminium alloy with 7% Si and a cast oxide layer was carried out by Haboudou et al. [181]. Braun [182] made a detailed study on butt welding of 6013 aluminium alloy sheet using a 3-kW Nd:YAG laser with two kinds of filler metals: gas atomized powders of aluminium alloys AlMg5, AlSi12, AlSi12Mg5, and AlSi10Mg, as well as powder mixtures of Al and Si and the binary alloys Al-5Mg, Al-5Zr, Al-5Cr, and Al-10Mn. The weld region exhibited a dendritic/cellular structure in the fusion zone and a partially melted zone adjacent to the fusion boundaries. The hardness of the fusion zone depended upon composition of the filler metals. Post-weld artificial aging improved the hardness due to the precipitation of strengthening phases. Optimum tensile properties were obtained with joints made with the filler powder AlSi12. The dispersoid forming elements Zr, Cr, and Mn added to a mixed Al-7Si powder did not prove beneficial in terms of weld quality. When exposed to an intermittent acidified salt spray fog, joints in the as-welded T4 and post-weld heat treated T6 conditions exhibited corrosion behavior similar to that of the base sheet in the tempers T4 and T6. As-welded 6013-T4 joints were susceptible to stress corrosion cracking when immersed in an aqueous solution of $0.6\text{M NaCl} + 0.06\text{M NaHCO}_3$. Sensitivity to environmentally aided cracking was associated with grain boundary precipitation in the heat affected zone.

Yue et al. [183] studied the influence of laser parameters on the welding behavior of a SiC particulate reinforced 2124 Al alloy composite using a pulsed Nd-YAG laser. Defects like solidification cracks and porosities were the common defects in laser welded Al-2124/SiC composite, formed mostly at high laser intensities and

short pulse durations. Wang et al. [184] have demonstrated the versatility of laser welding by carrying out in situ weld alloying and laser beam welding to join SiC reinforced 6061Al metal matrix composite using titanium as filler alloying element. Microstructural studies show that the detrimental needle-like aluminum carbides are completely eliminated and the central fusion joint consists of TiC, Ti₅Si₃, and Al₃Ti along with some large pores.

Microstructure and properties of 0.5-mm thick welded sheets of commercial purity titanium have been studied and compared following high vacuum electron beam welding, CO₂ laser beam welding and tungsten inert gas welding processes [185]. It was observed that electron beam welding is more suitable for defect-free welding of commercial purity titanium. Ti₃ Al–Nb alloy is one of the strong candidates for structural applications at moderate temperature in aerospace field because of its relatively low density and high elastic modulus. Wu et al. [186] welded Ti–24Al–17Nb (at.%) alloy with a fast axial flow type CO₂ laser of 3.0 kW rated power. The weld microstructure consisted primarily of ordered β phase (namely β 2 phase) and was independent of the laser parameters. The size and orientation of the solidification structures in the weld and bend ductility of the joints were related to the welding condition. The microstructure became coarser and the tendency for defect formation decreased as the heat input increased. The tensile strength and ductility of the joints were equal to that of the base material.

Laser welding of Ti-based alloys were extensively studied by Uenishi et al. [187], Li et al. [188] and Hsu et al. [149]. The microstructure of the fusion zone was strongly influenced by laser parameters. Hsu et al. [149] studied the effect of CO₂ laser welding of binary Ti₅₀Ni₅₀ and Ti_{49.5}Ni_{50.5} on shape-memory and corrosion characteristics of these alloys. Although martensite start (M_s) temperature was slightly lowered, no deterioration in shape-memory character of either alloy was observed. The same alloy registered satisfactory performance in potentiodynamic corrosion tests in 1.5 M H₂SO₄ and 1.5 M HNO₃ solutions. However, a significantly higher corrosion rate and a less stable passivity was noted in artificial saliva. On the other hand, the pseudoelastic behavior of the laser weld of Ti_{49.5}Ni_{50.5} alloy (in cyclic deformation) indicated that the stress (σ_m) required to form stress-induced martensite and permanent residual strain (ε_p) were higher after welding due to the more inhomogeneous nature of the weld metal.

Spot welding of Ta plates was performed with a pulsed Nd:YAG laser (50 W) coupled with a step index fiber. A series of spot welds was achieved with a peak power of 3 kW (i.e. a power density of $42 \times 10^9 \text{ Wm}^{-2}$) and pulse duration between 1 and 16 ms [189]. The presence of small and large key holes suggested that the key-hole geometry and solidification time primarily determined whether volume defects (porosity) would form and optimization of process parameters could minimize the tendency of defect formation.

Bead-on-plate welds were produced on 4-mm thick V-4Cr-4Ti alloy sheets using a 1.6 kW pulsed YAG laser with fibre-optic beam delivery [190]. The effect of process parameters (laser power, interaction time, welding atmosphere) on weld depth, porosity, and oxygen uptake was studied to determine optimum pulse

parameters as follows: 4 J/ms pulse energy, 3 ms pulse length, and 132 Hz pulse repetition rate.

Laser beam welding of Hastelloy X was performed using a 1.2 and 6 kW CO₂ laser with lap and butt joints [191]. Cracks in the fusion zone were observed which could be eliminated by changing the beam diameter and alignment. Metallurgical analysis using electron microscopes revealed pronounced signature of redistribution of alloying elements in the weld zone.

Song et al. [192] studied the weldability of AZ31B magnesium alloy sheets by laser-arc hybrid welding process. A sound overlap-welded joints of magnesium alloy AZ31B sheets without defects was obtained. Among the welding parameters, defocusing distance and laser-to-arc distance were key factors to affect the penetration depth and bead shape. It was also found that the cross section of hybrid overlap-welded joint assumed a “thumb pin” shape due to the nature of energy deposition in laser-arc hybrid welding. Hybrid overlap-welded joints actually comprises two parts: one due to laser irradiation alone, while the other due to the action of both laser and arc. The study showed that tensile strength and corrosion resistance of laser-arc hybrid welded AZ31B alloy was 80% equivalent to that of the base metal, respectively. In another attempt, Liming et al. [193] compared the weldability of AZ31B magnesium alloy using hybrid laser-TIG (LATIG) welding, laser beam welding (LBW) and gas tungsten arc (TIG) welding and found that the welding speed of LATIG was higher than that of TIG but comparable to LBW, and penetration of LATIG was twice that of TIG and four times that of LBW. In addition, arc stability was better in hybrid laser-TIG welding than TIG welding, especially at high welding speed and low TIG current. It was found that the heat affected zone of joint was only observed in TIG welding, and the size of the grains was evidently coarse.

Kim et al. [194] studied the welding of Cu₅₄Ni₆Zr₂₂Ti₁₈ metallic glass using pulsed Nd:YAG laser. It was observed that crystallization could be suppressed both in weldment and heat affected zone at a welding speed of 60 mm/min. On the other hand, crystallization areas with a band shape were observed at a welding speed of 20 mm/min.

Wang et al. [195] studied the scope of welding between SiC dispersed 6061 Al matrix composite. Formation of needle-like detrimental phases of Al₄C₃ following the partial or complete dissolution of SiC reinforcement particles in the central weld was a serious problem. The harmful needle-like carbide formation was avoided by addition of Ti as an alloying element in the composites [184]. Central fusion zone consisted of TiC, Ti₅Si₃, and Al₃Ti.

Sierra et al. [196] studied the weldability of a low carbon steel to 6,000 series aluminium alloy in key-hole welding mode using a continuous wave Nd:YAG laser. Defect-free welding can be obtained on overlapping Al + steel joints with the weld zone composed of solid solution of aluminium in iron and FeAl phases when penetration of steel in aluminium was below 500 µm. Embrittlement at the joining zone was observed, mainly located on the weld-aluminium interfaces comprising Fe₂Al₅ and/or FeAl₃ phases with thicknesses between 5 µm and 20 µm.

Majumdar et al. [197] developed crack-free weld between a commercially available Ti alloy (Ti-6 wt% Al-4 wt% V) and a wrought Al alloy (Al-1 wt%

Mg-0.9wt% Si). Intermetallic compounds (mainly TiAl and Ti₃Al) were formed in the fusion zone depending on the amount of Al and Ti melted by the laser. These intermetallic phases are very brittle and the solid-state cracks are formed near the Al side of the interface because of the stress developed after the solidification. In order to minimize the dissolution of Al in the fusion zone and to increase the toughness of the intermetallic phases, Nb foil is added as a buffer between the Ti alloy and Al alloy work pieces. It is observed that the partially melted Nb acts as a barrier to dissolve Al in the fusion zone and facilitates a good joining condition for welding of Ti alloy with Al alloy.

Mai and Spowage [198] studied welding of steel to Kovar, copper to steel and copper to aluminium using a 350-W pulsed Nd:YAG laser. Laser welding of steel and Kovar resulted in significant intermixing of both materials within the fusion zone. Although the steel plate was completely melted, a complete metallurgical bond could not be obtained at the interface between the Cu-plate and the weld metal, mainly due to the high thermal conductivity of copper. The weldability of copper to aluminium is regarded as relatively good. The Cu–Al phase diagram shows a wide range of Cu–Al phases that may be formed. In addition, non-equilibrium cooling conditions are known to promote the formation of a series of metastable phases. Under optimum processing parameters, crack-free welds between copper and Al 4047 were obtained.

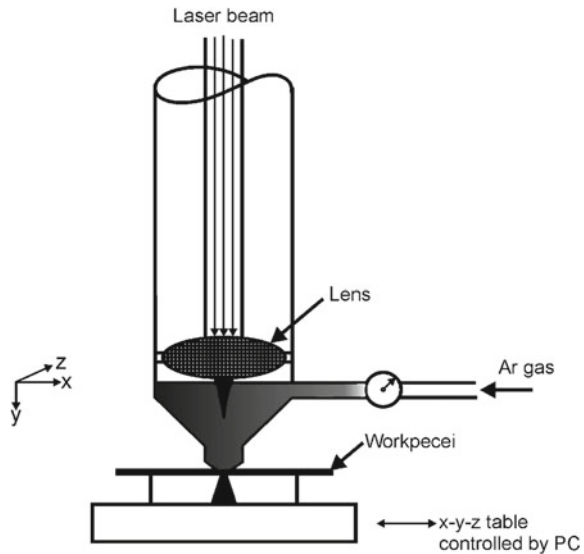
1.8 Laser Machining

Machining of materials can be achieved by laser-induced concomitant melting and evaporation from the surface or bulk of the work piece. A high power laser may be utilized to carry out drilling, cutting, cleaning, marking, and scribing up to a limited dimension or depth of all varieties of materials [2, 4]. In this section, the principle of different laser assisted machining processes would be discussed highlighting the scope/versatility of the processes emphasizing the recent advances and future scope of applications.

1.8.1 Laser Cutting

Cutting is the most widely practiced industrial application of laser among the machining operations. The advantages of laser cutting over other techniques are: flexibility, scope of automation, ease of control over depth of cut, cleanliness, non-contact processing, speed, amenability to a wide variety of materials (ductile/brittle, conductor/non-conductor, hard/soft), negligible heat affected zone, and narrow kerf [2]. Figure 1.15 shows the schematic of a laser assisted cutting setup. The specimen is fixed in X–Y sweeping stage. The laser beam is used to irradiate the material surface with a particular interaction time so as to cause controlled removal of solid from the surface. The main processing parameters for laser assisted cutting

Fig. 1.15 Schematic of laser assisted cutting setup [2]



are applied power density, interaction, time and shrouding environment. There are six different mechanisms for laser assisted cutting of materials, namely vaporization cutting, melting and blowing (or simply melting), burning and blowing, thermal stress cracking, scribing, and cold cutting [2].

1. Vaporization cutting

In vaporization cutting, the focused beam raises the surface temperature above the boiling point and generates a keyhole, which causes a sudden increase in absorptivity due to multiple reflections leading to quicker extension of the hole. As the hole or kerf deepens, vapor forms, ejects out of the hole or kerf, and stabilizes the molten walls of the hole. This method is more useful in cutting materials that do not melt such as wood, carbon, and plastic. The parameters controlling the laser cutting operation are beam diameter, laser power, traverse speed, gas composition, material thickness, reflectivity, and thermophysical properties of the work piece. Vaporization cutting of ceramics depends largely on the power density of the laser beam. Normally, the intensity should be near to or greater than 10^{12} W/m² for complete vaporization before cutting/evaporation.

2. Fusion cutting (melting and blowing)

In this process, a laser beam is used to melt the material and cutting is undertaken by blowing the molten material away with a sufficiently strong gas jet. This process requires only one tenth of the power for vaporization. If the gas (oxygen) reacts exothermically with the workpiece then another heat source is added to the process and is termed as reactive fusion cutting. Usually the reactive gas is oxygen or some other gas mixture containing oxygen. The burning reaction starts usually at the top when the temperature reaches the ignition temperature leading to the formation of

oxide that blows into the kerf and covers the melt. Formation of striation is a problem associated with reactive fusion cutting when the cutting speed is very slow. Chen and Siores [199] discussed the problem of striation formation in detail during the laser cutting process. Pietro and Yao [200] developed a transient 2-D model to investigate the effect of various CNC velocity profiles on the resulting cutting front temperature. It was shown that cutting efficiency increased with the cutting speed because of the greater energy coupling to the work piece. Steady-state cutting front temperature also increased with increasing cutting speed. Boundary encroachment and bulk heating effects (due to workpiece geometry) caused the front velocity to increase dramatically on approaching the edge of the workpiece so that the beam coupling was significantly reduced without changing the processing speed. A nonlinear velocity profile was evaluated via an optimization strategy that stabilized the cutting front temperature to its steady-state value. Duan et al. [201–203] developed a theoretical model for predicting the 3-D stationary geometry of the cutting front during laser assisted fusion cutting. The effect of various laser processing parameters, multiple reflections and inert gas pressure on the geometric shape of the cutting front and cut-edge quality were analyzed in detail.

3. Controlled Fracture

This approach is useful for cutting brittle material. During this process, laser beam heats a small volume of the surface causing it to expand and produce tensile stresses around the irradiated zone. If there is a crack in this space, it will act as a stress raiser, and cracking will continue in the direction of hot spot. The process requires very little power. The heat produced on the surface separates the substrate controllably along the moving path of the laser beam. Because the extension of the breaking frontier is larger than the movement of the laser spot, the actual fracture trajectory deviates from the desired trajectory while cutting a curve or an asymmetric straight line. To eliminate this deviation, the iterative learning control method is introduced to obtain the optimal laser beam movement path [204].

4. Scribing

During the process, a laser beam is used to weaken the structure by making a groove or line of holes following which it is mechanically broken. Absence of formation of debris and low heat affected zone are the advantages associated with this technique [2].

5. Cold Cutting

This is the process of breaking the bond of organic materials by irradiating it with excimer laser working in the ultraviolet region [2]. This process is useful in cutting plastic, machining of human hair, micro-surgery, and engineering with single cells, tumor surgery, etc. Correlation of cutting characteristics with laser parameters and analysis of process windows for laser cutting is essential to attain a defect-free cutting operation [205]. Experimental observations showed that the differences between upper and lower corner stresses are temporarily dependent on the passivation breakthrough caused by upper corner cracks. In a recent model on metal cutting with a gas assisted CO₂ laser, laser cutting is considered as a surface reaction and absorption

process that needs an adjusting parameter to represent the absorptivity for different materials at different incident angles [206]. Computation of the mass diffusion rate at the gas/solid boundary of the cutting front should include the exothermic heat released during cutting. It is shown that a very small level of impurity in oxygen exerts a significant influence on the cutting performance. Earlier, the combined effect of chemical reactions taking place between a gas jet and molten metal was considered adopting a laminar boundary layer approach [207]. Li et al. [208] presented an analytical model for laser cutting.

Laser parameters controlling the quality of cutting zone include laser power density, interaction time, position of the laser beam with respect to the surface, and the gas composition. The empirical relationship among laser power (P , W), sheet thickness (d , mm), cut width (s , mm), and cutting speed (V , mm/min) was established as: $P = 390d^{0.21} s^{0.01} V^{0.16}$ (ignoring variation of thermal properties of material with temperature) [209]. The composition of cutting gas also plays an important role in determining the quality of cut. It was found that high purity oxygen was conducive for better cutting performance as compared to inert gas. However, striation formation at the cut edge is often encountered during oxygen cutting of mild steel attributed to (1) cyclic variation in the driving force of the oxidation reaction owing to changes in the oxygen partial pressure in the melt zone melt (2) viscosity and surface-tension effects associated with melt removal [210].

Machinability of galvabond steel sheet with a good quality was achieved using continuous wave CO₂ laser by proper control of the cutting parameters [211]. Laser cutting was successfully applied for cutting of stainless steel, aluminium, and mild steel with a CO₂ laser and showed that laser cuts had narrower kerf width with better accuracy than that by mechanical cutting [212]. Metal matrix composites are difficult to machine. Pulsed laser cutting of Al–Li/SiC metal matrix composite was extensively studied by Yue and Lau [213] to optimize the process parameters to minimize the heat-affected zone, improve the quality of the machined surface, and predict the maximum depth-of-cut for the composite. The effects of femtosecond laser machining on surface characteristics and subsurface microstructure of a Nitinol alloy were studied by Huang et al. [214].

Superalloys have high strengths at elevated temperatures, which make them attractive for various structural applications at high temperature. The same property makes these materials difficult to machine at room temperature due to excessive tool wear and poor surface finish. Laser assisted machining offers the ability to machine superalloys more efficiently and economically by providing the local heating of the workpiece prior to material removal by a single point cutting tool. The machinability of Inconel 718 under varying conditions was evaluated by Anderson et al. [215]. With increasing material preheating temperature from room temperature to 620°C (by laser heating), the benefit of laser assisted machining was demonstrated by a 25% decrease in specific cutting energy, 2–3-fold improvement in surface roughness and 200–300% increase in ceramic tool life over that in conventional machining. Moreover, an economic analysis shows significant benefits of laser assisted machining of Inconel 718 over conventional machining with carbide and ceramic inserts.

One of the most useful and niche applications of laser is cutting of ceramics. Ceramics have excellent resistance to heating, wear, and corrosion, and are routinely used in many industrial applications. However, the high hardness and brittleness of ceramics makes them difficult and expensive to machines using conventional cutting methods or tools. Laser cutting provides a good means for cutting of ceramics in non-contact mode with excellent precision. In laser machining of ceramics, the removal process is a combination of several mechanisms, the extent and magnitude of each varying according to the nature and power of the laser beam and the type of ceramic substrate being machined. Basically, the machining process consists of three inherent stages, i.e., vaporization cutting, melting, and ejection and controlled fracture [216]. However, the success of laser cutting of ceramics crucially depends on resolving a few fundamental problems like formation of cracks during cutting due to thermal shock. Lu et al. [217] studied the problem of cracking of ceramic plates during laser assisted cutting and identified that the most relevant parameters for laser cutting were laser power (P) and scan speed (v), specific heat (c), conductivity, (k) and thermal expansion coefficient (α). Tsai and Chen [218] attempted synchronous application of Nd:YAG and CO₂ laser for laser cutting of thick ceramic substrates by controlled fracture. The focused Nd:YAG laser was used to scribe a groove crack on the surface of the substrate and defocused CO₂ laser was utilized to apply large thermal stress. During dual beam irradiation, thermal stress concentration along the tip of the groove-crack would make it extend through the substrate, followed by the substrate separating along the moving path of the laser beam in a controlled manner. Under an output power of 60 W for both CO₂ laser and Nd:YAG laser, the maximum cutting speed achieved was 1.5 mm/s for a thick alumina sample. The temperature and stress distributions were analyzed by using the finite element software ANSYS and microstructure (micro-mechanism of the fracture process) was studied by scanning electron microscopy. The relationships among laser power, cutting speed, and specimen geometry/thickness were determined from the experimental and stress analysis. In this regard, Tsai and Chen [219] proposed a new image processing system to determine the laser movement path by iterative path revision algorithm useful for monitoring laser assisted cutting.

The effect of laser power, scan speed, mode of cutting, and shield gas composition on cutting of thick ceramic tiles using continuous wave CO₂ laser was studied by Black and Chua [220] and Black et al. [221]. Crack formation was one of the major problems associated with the cutting process. Large thermal gradient between the cut zone and associated glazed zone was responsible for the crack formation. Proper choice of laser parameters was essential to allow sufficient time to cool and minimize the tendency for crack formation.

Rebro et al. [222] evaluated the processing conditions for a defect-free laser assisted machining of pressureless sintered mullite ceramics which otherwise is difficult due to its low thermal diffusivity and inferior tensile strength. To achieve the benefits of strength reduction due to softening of mullite, laser power of 170–190 W provided positive results. These settings allowed machining of semicontinuous chips, significant reduction in specific cutting forces, increase in tool life, and retention of surface characteristics of the workpiece. Numerical modeling of workpiece temper-

ature along with experimental measurement by a pyrometer was performed to determine the temperature at the material removal zone during laser assisted machining and to analyze the temperature gradient information for detecting the onset of cracking. With a designed gradual heating method, laser assisted machining of mullite has been successfully performed without inducing any surface or subsurface cracks and at the same time, extending the tool life of carbide tools and producing good surface integrity. Graff and Meijer [223] reported on CO₂ laser cutting of newly developed materials (synthetic aluminium laminates) for the aeronautic and automotive industry at the same speed as homogeneous aluminum alloys with the presence of some damage. A dedicated computer simulation model was also developed using appropriate mass, power, and force balance equations considering splitting of the laminate in several horizontal layers according to the concerned thermophysical and optical properties.

1.8.2 Laser Drilling

Drilling is a machining operation with a stationary workpiece to produce usually circular and vertical holes on the workpiece. High power CO₂ laser or Nd:YAG laser may be used to drill a hole. Laser drilling can be done both in pulsed and continuous wave modes with suitable laser parameters. The advantage of using laser is that it can drill holes not only vertically but also at an angle inclined to the surface (e.g. fine lock pinholes in Monel metal bolts). Mechanical drilling is slow and causes extrusions at both ends of the hole that have to be cleaned. Mechanical punching is fast but is limited to shallow with greater than 3 mm in diameter. Electrochemical machining is quite a slow process (180 s/hole) though produces a neat and precise hole. Electro discharge machining is expensive and slow with a typical rate like 58 s/hole. Electron beam drilling is fast at 0.125 s/hole but needs a vacuum chamber and is more expensive than a Nd:YAG laser processing. In comparison, a Nd:YAG laser can produce a hole in 4 s to outsmart all other methods [2].

The ability to machine very small features like holes into a metal, ceramic, semiconductor, or polymer sheet/film by laser ablation with an unmatched precision, accuracy, and speed has opened a very useful scope of application of laser material processing in the microelectronic industry. For instance, holes with a diameter of 300 nm and depth of 52 nm could be drilled in metal films with minimum distortion and heat affected zone using 200 fs and 800 nm pulses from a Ti:sapphire laser focused to a spot size of 3000 nm. Lehane and Kwok [224] have developed a novel method for improving the efficiency of laser drilling using two synchronized free-running laser pulses from a tandem-head Nd:YAG laser capable of drilling through 1/8-in-thick stainless steel targets at a standoff distance of 1 m without gas-assist. The combination of a high-energy laser pulse for melting coupled with a properly tailored high-intensity laser pulse for liquid expulsion results in efficient drilling of metal targets. The improvement in drilling is attributed to the recoil pressure generated by rapid evaporation of the molten material by the second laser pulse. Similarly,

Zhu et al. [225] have carried out a detailed experimental study of drilling submicron holes in thin aluminum foils with thicknesses ranging from 1.5 to 50 μm , and W, Mo, Ti, Cu, Fe, Ag, Au, and Pb foils of 25 μm thickness with femtosecond Ti:sapphire laser pulses of 800 nm width. The influence of laser parameters and material properties on hole drilling processes at submicron scale has been examined and a simple model to predict the ablation rate for a range of metals has been developed. Laser precision machining has been applied to fabricate metallic photonic band-gap crystals operating in the microwave frequency [226]. Transmission measurements showed that the periodic crystals exhibited a cutoff frequency in the 8–18 GHz range allowing no propagation below this level. Furthermore, the cutoff frequency could easily be tuned by varying the interlayer distance or the filling fraction of the metal. Combination of plates with different hole-diameters creates defect modes with relatively sharp and tunable peaks.

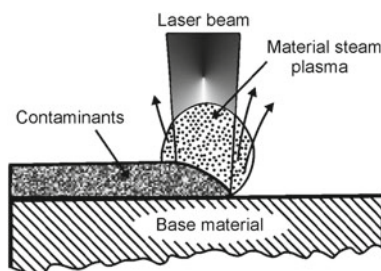
The microelectronics industry is moving toward smaller feature sizes so as to improve design and performance and lower cost. Small distances between chips together with the short interconnection routes are conducive for faster operation. Laser processing for via generation, direct pattern processing, image transfer, contour cutting, and trimming now find increasing application in the microelectronic packaging industry. On the other hand, smaller space between conductive patterns increases the risk of short circuits (caused by pattern faults, solder bridges, migration, etc.) that emphasizes the need to ensure reliability of laser processing [227].

The microelectronics industry is moving toward smaller feature sizes so as to improve the design and performance and lower cost. Small distances between chips together with the short interconnection routes are conducive for faster operation. Laser processing for via generation, direct pattern processing, image transfer, contour cutting, and trimming now find increasing applications in the microelectronic packaging industry. On the other hand, smaller space between conductive patterns increases the risk of short circuits (caused by pattern faults, solder bridges, migration, etc.) that emphasizes the need to ensure reliability of laser processing.

For micromachining, femtosecond pulses offer an advantage over current technology of employing nanosecond pulses because of the reduced effects of thermal diffusion [228]. Using the femtosecond pulses, holes with a diameter of 300 nm, roughly 10% of the spot size was produced, whereas the smallest diameter made using the nanosecond pulses was roughly 60% of the spot size. The depth of the femtosecond hole was 52 nm. Also the fact that the fluence threshold is lower for femtosecond pulses than for nanosecond pulses, which is useful for certain machining situations, such as medical surgery, where low fluences are desirable to reduce the effects of collateral damage, that is, damage to tissue located outside the desired region.

Demands for producing micro crack-free, high quality and high-aspect ratio microholes and microfeatures in glass substrates have been increasing for a number of applications such as in MEMS device packaging, optical fiber alignment, mini-vision systems, and microelectronic packaging. However, due to the poor thermal properties of most glasses the fabrication of finely machined features, e.g. grooves, microholes etc. has been a challenging task. Different types of glass materials were

Fig. 1.16 Schematic of laser assisted cleaning



machined by using short pulse solid-state lasers with pulse duration in the ns to fs range [229].

1.8.3 Laser Cleaning

Removal of small particles or continuous layers from a metal surface can be carried out by laser beam using a selected area irradiation at an optimum combination of incident power, interaction/pulse time, and gas flow rate (that sweeps the dislodged atoms from the surface). Figure 1.16 schematically shows the mechanism of laser cleaning. At the initial stage, a plasma plume is formed due to ionization of the atoms vaporized from the surface and blocks the beam-surface contact. As the irradiation stops, the temporary compression on the surface changes into tension and causes spallation of the oxidized layer. A dramatic improvement of cleaning efficiency in terms of area and energy is possible when laser beam irradiates the workpiece at an oblique or glancing angle of incidence rather than direct or perpendicular irradiation of the surface. The influence of pulsed laser irradiation on the oxide scale removal from the surface of stainless steels oxidized using a pulsed Nd:YAG laser was investigated by Psyllaki and Oltra [230]. At an appropriate angle of incidence, laser irradiation with energy density of $\sim 10^4 \text{ J/m}^2$ resulted in expulsion of the oxide layer without any material removal from the underlying metal. The side wall and bottom polymers resulting from reactive ion etching of via holes can be removed by a non-contact dry laser cleaning technique using pulsed excimer laser irradiation [231].

Similarly, laser cleaning is capable of removing the polymers by subthreshold ablation, even at fluences limited by the damage threshold ($= 2,500\text{--}2,800 \text{ J/m}^2$) of the underlying Al–Cu metal film with titanium nitride (TiN) anti-reflective coating. Comparing ablation results obtained using Nd-YAG laser and excimer laser shows that although the shorter 7 ns Nd-YAG laser pulse gives a greater etch thickness than the 23 ns excimer laser pulse, it also tends to damage the metal films and the silicon substrates of the via wafers more easily.

Single crystal SiC substrate was successfully photo-etched at a remarkably high etch rate of 35 nm/s by (133, 141, 150, 160, 171 and 184–266 nm) multi-

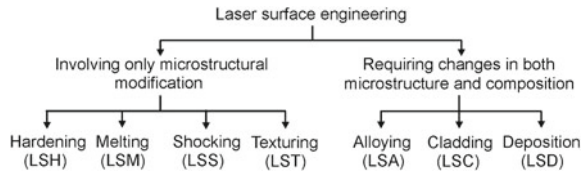
wavelength laser ablation, combined with a chemical posttreatment in a solution of $\text{HCl} + \text{H}_2\text{O}_2 + \text{H}_2\text{O}$ and $\text{HF} + \text{H}_2\text{O}$ [232]. The analysis of the etched samples by scanning electron microscopy and scanning probe microscopy indicated that an array of square holes having well-defined patterned structures and clean substrate surfaces were obtained. X-ray photoelectron spectroscopy analysis indicated that the SiC samples etched by multi-wavelength laser have a similar stoichiometry after chemical posttreatment as the virgin SiC. The mechanism of high-quality ablation using multi-wavelength laser was discussed and compared with that for ablation using 266 nm single wavelength. The chemical post-treatment contributed to removing the residues from the laser photolysis of SiC.

1.9 Laser Surface Engineering

Failure of engineering components or materials due to chemical (corrosion and oxidation) or mechanical (wear and erosion) interaction is most likely to initiate from the surface because both external and internal surfaces/interfaces are more prone to environmental degradation, and intensity of externally applied load is usually the highest at the surface [233]. The engineering solution to minimize or eliminate such surface initiated failure lies in tailoring the surface composition and/or microstructure of the near-surface region of a component without affecting the bulk [2, 3, 233–235]. In this regard, the more commonly practiced or conventional surface engineering techniques like galvanizing, diffusion coating, carburizing, and nitriding possess several limitations like high time/energy/material consumption, poor precision and flexibility, lack in scope of automation/improvisation, and requirement of complex heat treatment schedule. Furthermore, thermodynamic constraint of restricted solid solubility and kinetic limitation of thermally activated solute transport to solid-state diffusion impose further limits to the level of improvement possible through these conventional or near-equilibrium processes [234, 235].

In contrast, surface engineering methods based on application of electron, ion, and laser beams are free from many of the above restrictions of equilibrium surface engineering methods. A directed energy electron beam is capable of intense heating and melting the surface of all engineering solids [236]. However, electron beam delivers a Gaussian energy deposition profile, and hence, is more suitable for deep penetration welding or cladding of similar or dissimilar solids (Fig. 1.3). Moreover, the scope of generation of X-ray by rapid deceleration of high-energy electrons impinging on a solid substrate necessitates adequate safety provisions to prevent possible health hazards. On the other hand, ion beam processing offers practically an unlimited choice, flexibility, and precision of tailoring the surface composition and microstructure by implantation of a single or multiple elements that has otherwise no or restricted solid solubility in a given substrate [6, 3, 237]. However, the peak concentration of implanted species, like the energy deposition peak in electron beam irradiation, lies underneath and does not coincide with the surface (Fig. 1.3b, c). Furthermore, the requirements of an expensive ionization chamber,

Fig. 1.17 General classification of laser surface engineering [113]



long beam delivery system, and huge time needed to implant on a large surface area are serious impediments against large-scale commercial exploitation of ion beam assisted surface engineering. Laser circumvents the majority of the limitations cited above with regard to both conventional and electron/ion beam assisted surface engineering methods and offers a unique set of advantages in terms of economy, precision, flexibility, and novelty (thermodynamic and kinetic) of processing and improvement in the surface-dependent properties of interest [1–4]. One of the major advantages of laser in surface engineering is its exponential energy deposition profile vis-à-vis the Gaussian profile of that in electron or ion beam irradiation (Figure 1.3).

Laser surface engineering enables delivery of a controlled quantum of energy (10^4 to 3×10^5 J/m²) or power (10^8 – 10^{11} W/m²) with precise temporal and spatial distribution either in pulses (10^{-3} to 10^{-12} s) or continuous wave (CW). The advantages of laser surface engineering include an extremely fast heating/cooling rate (10^4 – 10^{11} K/s), very high thermal gradient (10^6 – 10^8 K/m), and ultra-rapid resolidification velocity (1 – 30 m/s), inducing possibility of development of novel microstructure and/or composition in the near-surface region with large extension of solid solubility and formation of metastable including nanocrystalline and amorphous phases [233–235].

Figure 1.17 presents a brief classification of different laser surface engineering methods that involve mainly two types of processes. The first type is meant only for microstructural modification of the surface without any change in composition (hardening, melting, remelting, shocking, texturing, and annealing), while the second involves both microstructural as well as compositional modification of the near-surface region (alloying, cladding, etc.).

1.9.1 Laser Transformation Hardening

Transformation hardening is a standard heat treatment for ferrous alloys (steel, cast iron, etc.) that involves heating to austenite (face centered cubic) phase and subsequent quenching to ambient or subambient temperature to enforce a shear-induced austenite to martensite (body centered tetragonal) transformation. In laser transformation hardening, only a thin surface layer of the substrate (instead of the entire bulk) is rapidly heated to the austenite phase field followed by rapid self-quenching to produce the desired martensitic microstructure [238]. Heating and cooling rates of 10^4 K/s or greater are typical of the laser surface hardening process and the entire

thermal cycle in the irradiated volume may be accomplished in less than 0.1 s. The application of high power lasers in surface engineering is a well-known process that has been in vogue over the past two decades and is now revolutionizing automobile and aerospace industries. Dutta Majumdar and Manna [239] have presented a detailed review on the fundamentals of laser hardening, associated benefits compared to the conventional hardening techniques.

1.9.2 Laser Surface Melting

Laser surface melting is another important and effective technique primarily to modify the microstructure of the near-surface region. The advantages of laser surface melting lie on microstructural refinement and homogenization of microstructure. Laser surface melting of 440C martensitic stainless steel was found to be more effective in improving the corrosion resistance (in NaCl solution) by carbide refinement, while laser transformation hardening was useful in enhancing the cavitation erosion resistance by formation of an appropriate amount of martensite and austenite [240, 241]. Laser surface melting has been proven to be an effective route in desintization of AISI 304 stainless steel by dissolving the carbides formed and suppression of its re-precipitation due to rapid quenching and homogenizing the microstructure leading to a significant improvement in corrosion resistance [242, 243]. Laser surface melting of DIN X42Cr13 samples showed a higher abrasive wear resistance than the same after tempering treatments due to strain-induced transformation of austenite into martensite and the work hardening of austenite during the wear tests [244]. Wilde et al. [245] showed that laser surface melting of AISI 4135 low alloy steel resulted in reduction in the hydrogen absorption kinetics as measured by the permeation test, and an improved resistance to hydrogen-induced fracture in the slow strain rate tensile test under galvanostatic charging conditions.

Laser surface melting was also proven to be an important technique for tailoring the surface properties of Al, Ti, Cu, Mg, and other important nonferrous metals and alloys to extend the service life of components. Laser surface melting of 7075-T651 Al alloy using an excimer laser was found to improve the resistance to stress corrosion cracking attributed to dissolution of grain boundary precipitates and supersaturation of solutes with the matrix making it more noble [246]. Laser surface melting of 2024-T351 aluminium alloy using a continuous wave CO₂ laser was found to improve its uniform corrosion resistance and pitting corrosion resistance attributed to homogenization of microstructure [247]. It is also an effective route in improving high temperature oxidation resistance [248]. Wong et al. [249] reported that the corrosion behavior of laser surface melted Al–Si alloy (using a continuous wave CO₂ laser) was significantly improved in 10% H₂SO₄ and 10% HNO₃ solutions, though similar level of improvement was not observed in 10% HCl+5% NaCl solution. It was also proven to be an effective route in improving wear resistance because of microstructural refinement and improved microhardness achieved by laser surface melting [250]. Watkins et al. [251] melted the surface of a series of Al-transition

metal alloys (Al–Cu, Al–Si, Al–Zn, Al–Fe) and obtained unique microstructural and compositional characteristics including improved hardness, wear and pitting corrosion resistance using a selected set of laser parameters. SiC dispersed Al alloy composite is the most promising class of metal-matrix composite for applications in automobile and aircraft industries. However, these composites undergo severe degradation in chloride containing environment.

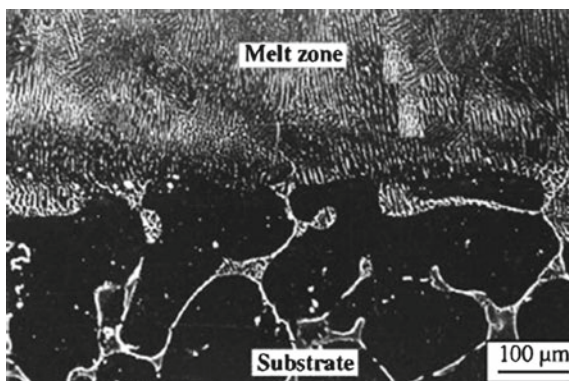
Vanderberg and Draper [252] laser surface melted commercial Al bronzes (containing 5 at% Fe, 13–28 at% Al) and found a variety of phases formed in the near-surface region. The microstructure consisted of α -phase (fcc solid solution), β_1 phase (product of ordering transformation of the high temperature disordered bcc phase β .) and even β phase (martensite formed by shear transformation on quenching). Rapid quenching in laser treatment also resulted in β_1 retention (by suppressing of martensite change) at Al concentration that was lower than what was usually observed with splat-quenching experiments.

Magnesium and its alloys are widely used in automotive and aerospace applications because of their light weight. However, poor wear and corrosion properties are of serious concern for its application as structural components. Laser surface melting of magnesium and its alloys were reported to be effective to refine the microstructure and improving corrosion resistance in AZ91D/AM60B [253], AZ91 [254], Mg-ZK60 [255] and other commercial Mg-based alloys [256]. Detailed studies on kinetics and mechanism of laser-surface-melted MEZ (a Mg–Zn alloy) were reported by Dutta Majumdar et al. [257]. Figure 1.18 shows the cross-section of the laser surface melted MEZ alloy, lased with a power of 2 kW and scan speed of 200 mm/min, consisting of fine columnar grains growing epitaxially from the liquid–solid interface [257]. The underlying substrate grains are significantly coarser with grain boundaries decorated with thick films of Mg/Zr/Ce-rich compound (confirmed by energy dispersive spectroscopy). Furthermore, the melted zone–substrate interface is crack/defect-free and well compatible with practically with no noticeable amount of heat-affected zone. A detailed evaluation of mechanical property shows that microhardness of the melted zone has significantly increased by 2–4 times (85–100 VHN) than that of the substrate (35 VHN) primarily due to grain refinement and solid solution hardening. While average microhardness varies with the concerned laser parameters, the maximum microhardness is achieved following laser surface melting with a power of 1.5 kW power and 200 mm/min scan speed. A detailed study of pitting corrosion shows that both the extent and rate of pitting are significantly reduced following laser surface melting.

Yu et al. [258] surface melted Mg–SiC (17 vol.%) composite using KrF excimer laser with Ar and N₂ as shrouding environment and achieved considerable improvement in corrosion resistance in 3.56 % NaCl solution primarily due to microstructural refinement. Similar surface melting in N₂ atmosphere improved the corrosion resistance further because of the formation of magnesium nitrides.

Laser surface melting of Ti–6Al–4V in nitrogen atmosphere leads to formation of a defect-free nitride zone consisting of TiN dendrites in α -Ti matrix. An increased surface roughness with a periodic texturing was noted on the nitrified surface [259, 260]. The residual stress on the surface nitrified zone was found to vary from

Fig. 1.18 Scanning electron micrograph of the cross-section of laser-surface-melted MEZ sample (lased with a power of 2 kW and a scan speed of 200 mm/min). The defect-free interface with significant grain refinement in the laser-melted zone may be noted [257]

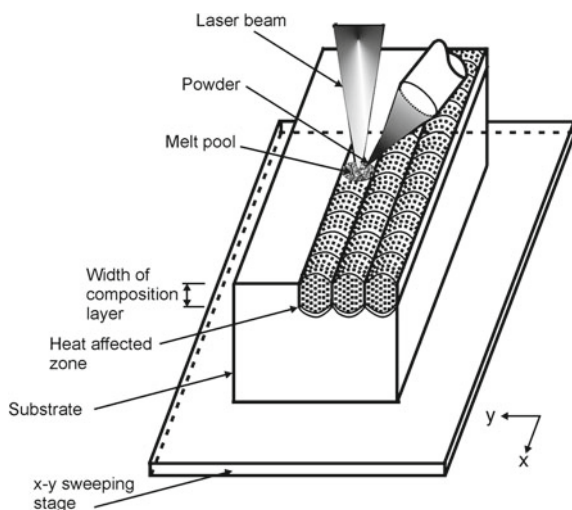


tensile to compressive. The residual compressive stress was developed when applying a high power and a very low gas flow rate. A significant improvement in microhardness of the nitrided zone is achieved (600–1,200 VHN) as compared to 280 VHN of as-received Ti–6Al–4V substrate. Pitting corrosion resistance in Hank's solution was also found to be improved due to laser gas alloying of Ti–6Al–4V with nitrogen.

1.9.3 Laser Surface Alloying

Laser surface alloying involves melting of alloy ingredients (either pre-deposited or simultaneously added in the form of powder or wire) along with a part of the underlying substrate to form an alloyed zone for improving the surface dependent engineering properties of substrate [261–264]. Figure 1.19 illustrates the scheme of laser surface alloying with a continuous wave laser. It includes three major parts: a laser source with a beam focusing and delivery system, a microprocessor controlled sweeping stage where the specimen is mounted for lasing and the arrangement for delivering the alloying ingredients in the form of powder. The process includes melting of the alloy ingredient along with the part of substrate, subsequent inter-mixing, and rapid solidification to form the alloyed zone confined to a very shallow depth from the surface. A 20–30% overlap of the successive molten/alloyed track is intended to ensure microstructural/compositional homogeneity of the laser treated surface in laser alloyed zone that has a composition distinctly different from that of the underlying base substrate. The sweeping stage ($x - y$ or $x - y - z - \theta$) allows laser irradiation of the intended area of the sample surface at an appropriate rate and interaction time/frequency. The depth, chemistry, microstructure, and associated properties of the alloyed zone depend on the suitable choice of laser/process parameters, i.e., incident power/energy, beam diameter/profile, interaction time/pulse width, pre- or co-deposition thickness/ composition, and concerned physical properties

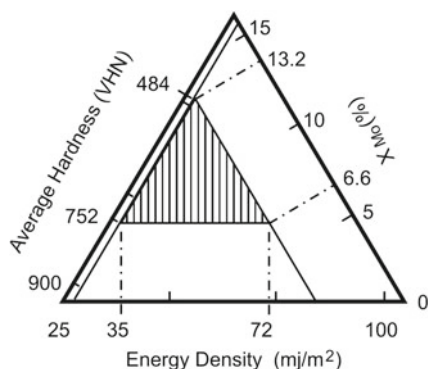
Fig. 1.19 Schematic of the experimental setup for laser surface alloying and the stages of irradiation, melting, intermixing, and solidification involved in laser surface alloying



like reflectivity, absorption coefficient, thermal conductivity, melting point, and density.

Dutta Majumdar and Manna [265] observed a significant improvement in pitting corrosion resistance of AISI 304 stainless steel by laser surface melting of plasma spray deposited Mo. Figure 1.20 shows the optimum conditions (shaded region) for the formation of a homogeneous microstructure and composition for improvement in pitting corrosion resistance and mechanical property [265]. Potentiodynamic anodic polarization tests of the substrate and laser surface alloyed samples in 3.56 wt. % NaCl solution (both in forward and reverse potential) showed that the critical potential for pit formation (E_{pp1}) and growth (E_{pp2}) were significantly (2–3 times) improved from 75 mV(SCE) in the substrate to 550 mV(SCE) after laser surface alloying. E_{pp2} has also been found to be nobler in as-lased specimens than that in the stainless steel substrate. The poor pitting corrosion resistance of the plasma sprayed stainless steel samples (without laser remelting) was due to the presence of surface defects present in the plasma deposited layer. Standard immersion test was conducted in a 3.56 wt. % NaCl solution to compare the effect of laser surface alloying on the pitting corrosion resistance. It was concluded that laser surface alloying was imparted an excellent microhardness, pitting corrosion, and erosion–corrosion properties to austenitic stainless steel due to Mo both in solid solution and as precipitates. In the past, attempts were made to enhance oxidation resistance property by laser surface engineering techniques [77]. The effect of laser surface alloying of 2014–T6 (Al–4.65Cu–0.5Mg–0.8Si wt.%) Al-alloy with 25Cr–75Al, 75Cr–25Al, 25W–75Al, 75W–25Al, 8Al–72Zr–20Ni and 35Al–50Ti–15Ni powder mixtures using an ElectroX 2 kW continuous wave CO₂ laser on the microstructure and corrosion behavior were studied [251]. Jain et al. [266] vacuum deposited Cr film (thickness varying from 650 to 1350 nm) on Al substrate and irradiated with single pulses (with a full width at half-maximum of 7 ns) Nd-glass laser operating in

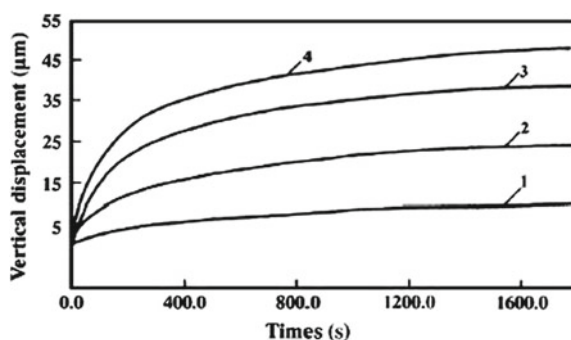
Fig. 1.20 Optimum conditions (*shaded region*) for the formation of a homogeneous microstructure and composition in laser-surface-alloyed AISI 304 stainless steel with Mo [265]



a TEM00 mode at peak power densities of 6,000 – 15,000 GW/m² in air. Almost complete removal of chromium at 8,000 J/m² is followed by the rapid diffusion of chromium. Similar attempt of laser surface alloying of Al with Mo was undertaken by laser surface alloying with a composition ranging from 14.8 to 19.1 wt.% Mo and resulted in VHN 85–100 in hardness and 84–92 GPa in Young's modulus (determined by nano indentation [267]). Tang et al. [268] observed that laser surface alloying of Mg–Ni–Al bronze with Al was more effective in enhancing corrosion and cavitation erosion resistance in a 3.56 wt.% NaCl solution than that after laser surface melting. Improvement in wear resistance of Al alloys seems to necessitate addition of ceramic or intermetallic particles by laser surface cladding or alloying. Dutta Majumdar et al. [269] developed a titanium boride-dispersed Al-based metal matrix composite on the surface of pure Al by melting the surface of as-received substrate using a continuous wave CO₂ laser and simultaneous deposition of a mixture of K₂TiF₆ and KBF₆ (in the weight ratio of 2:1) through an external feeder (at a feed rate of 4 g/min).

The microstructure of the surface layer consisted of uniformly dispersed titanium boride (TiB) and titanium diboride (TiB₂) particles in grain refined Al matrix [269]. Figure 1.21 shows the variation of wear loss (in terms of depth of wear) as a function of time for as-received and laser composite surfaced Al with TiB₂ (lased with a power of 1.2 kW and scan speed of 700 mm/min) using a friction and wear monitor unit with an applied load of 500 and 900 g, respectively. It is evident that the rate of wear increases both with time and applied load. In pure Al (curves 3 and 4), the wear rate is very high at the initial stage of wear (up to 5 min) following which the same decreases. On the other hand, the magnitude and rate of wear is significantly lower in laser composite surfaced Al than that of as-received Al, though the same increases with increase in load for both as-received and laser composite surfaced Al with TiB₂. The kinetics of wear was, however, found to vary with laser parameters. Maximum wear resistance was achieved in laser composite surfaced Al lased at a power of 1.2 kW and scan speed of 700 mm/min. It is relevant to mention that wear resistance of the composite layer was found to increase with increase in microhardness of the composite layer. Hence, the improved wear resistance of laser composite surfaced Al was attributed to improved microhardness of the composite layer because of both

Fig. 1.21 Cumulative wear loss (in terms of vertical displacement) as a function of time for as-received Al with an applied load of 500 g (plot 3), 900 g (plot 4) and laser composite surfaced Al with TiB_2 (with a power of 1.2 kW and scan speed of 700 mm/min) with an applied load of 500 g (plot 1), 900 g (plot 2) using a friction and wear monitor unit [269]



grain refinement and precipitation of fine and hard TiB_2 and TiB particles in the matrix.

Aihua et al. [270] developed a graded coating consisting of a Ni-clad Al bond layer, a 50 wt.% Ni-clad Al + 50 wt.% ($\text{Al}_2\text{O}_3 - 13 \text{ wt.}\% \text{TiO}_2$) intermediate layer and an $\text{Al}_2\text{O}_3 - 13 \text{ wt.}\% \text{TiO}_2$ overlayer (or ceramic layer) on an Al-Si alloy substrate by plasma spraying followed by laser surface remelting. While the plasma-sprayed coatings seem prone to spallation at the different depths originating from macrocracks in the ceramic layer during thermal cycling, the laser-remelted coatings, containing a network of microcracks in the ceramic layer reveal a significantly reduced tendency of spallation at the interface between the intermediate and bond layer. Thus, laser remelting improved the spalling resistance of plasma-sprayed coating to thermal shock, though cracking due to thermal shock remains a problem to be solved. Uenishi et al. [271] obtained Al_3Ti -dispersed intermetallic-matrix composite on Al by laser surface cladding.

Dutta Majumdar and Manna [272] attempted to enhance the wear and erosion resistance of Cu by laser surface alloying with Cr (electrodeposited with 10 and 20 μm thickness, t_z). Figure 1.22 shows the scanning electron micrograph of the top surface of laser surface alloyed copper with chromium showing the presence of fine chromium of dimensions ranging from 100 to 500 nm in grain refined copper matrix. Chromium was found to be present both in solid solution and in the form of precipitates [272]. Laser surface alloying extended the solid solubility of Cr in Cu to a maximum of 4.5 wt. %. The microhardness of the alloyed zone was found to improve significantly (as high as 225 VHN) following laser surface alloying as compared to 85 VHN of the base metal. Since hardness is related to Cr present in solid solution and dispersed as precipitates in the matrix, the variation of average microhardness of the alloyed zone as a function of the total Cr content, Cr dissolved in solid solution or volume fraction of Cr precipitated shows that hardness increases with all these microstructural factors, especially with the degree of solid solubility extension of Cr in Cu. Figure 1.23 shows the variation of scratch depth as a function of load for pure Cu as well as laser surface alloyed Cu with Cr subjected to scratching with an oscillating steel ball in a computer-controlled scratch tester. It is evident that the rate of increase of scratch depth with both load and number of scratches is much higher in

Fig. 1.22 Scanning electron micrograph of the top surface of laser surface alloyed Cu with Cr (lased with a power density of $1,270 \text{ MW/cm}^2$, interaction time of 0.08 s at a predeposition thickness of $20 \mu\text{m}$) [272]

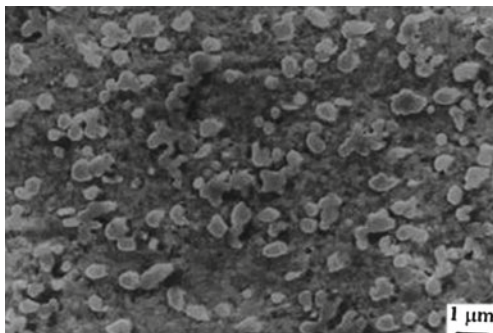
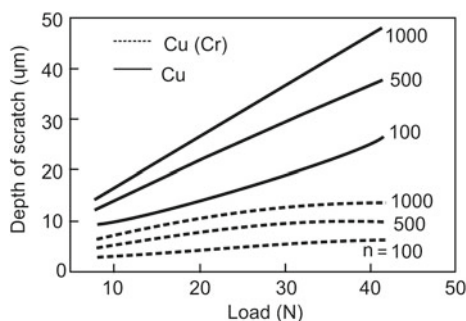


Fig. 1.23 Variation of scratch depth (z_{sc}) with (a) L and (b) n_{sc} for pure Cu (broken line) and laser alloyed Cu(Cr) (continuous line), respectively [272]



pure Cu than in laser-alloyed sample. Figure 1.24 compares the kinetics of material loss (Δm) of laser surface alloyed Cu (lased with 1590 MW/m^2 power, 0.08 s interaction time, with a pre-deposit thickness of $20 \mu\text{m}$) with that of Cu as a function of time (t) under an accelerated erosive wear condition conducted both at room and high temperature in a slurry bath containing 20 wt. \% sand. Laser surface alloying has significantly decreased the kinetics of erosion loss in laser surface alloyed Cu than in pure Cu under comparable conditions. Though the extent of material loss increases with an increase in temperature for both pure Cu and laser alloyed Cu, the rate of erosion loss in laser alloyed specimen is negligible as compared to the substantial change in erosion loss with temperature change for pure Cu, especially beyond 370 K .

Laser surface alloying of Ti with Si, Al, and Si + Al (with a ratio of 3:1 and 1:3, respectively) was conducted to improve the wear and high temperature oxidation resistance of Ti [273–275]. Figure 1.25 reveals a typical hypereutectic microstructure on the top surface of the alloyed zone consisting of uniformly distributed faceted Ti_5Si_3 phase in a two-phase eutectic aggregate of $\alpha\text{-Ti}$ and Ti_5Si_3 [276]. The high volume fraction of the primary phase and degree of fineness of the eutectic products signify complete dissolution and uniform intermixing of Si in the alloyed zone, and a rapid quenching experienced by the latter, respectively. Subsequent oxidation studies conducted at $873\text{--}1,023 \text{ K}$ showed that laser surface alloyed Ti with Si and Si + Al significantly improved the isothermal oxidation resistance (Fig. 1.26). In addition to

Fig. 1.24 Comparison of material loss per unit area (Δm) of Cu(Cr) with that of Cu as a function of (a) time (t), and (b) temperature (T) due to erosion in flowing SiO_2 -dispersed water medium [272]

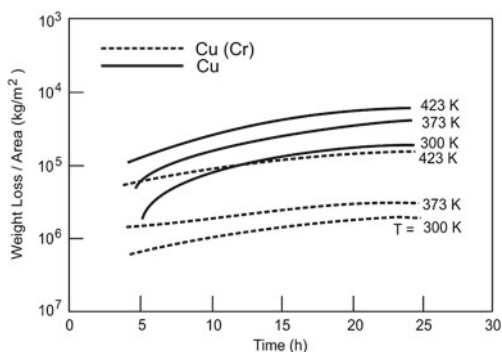


Fig. 1.25 Scanning electron micrograph (SEM) of the top or laser alloyed surface of Ti with Si (lased with a power of 4 kW, scan speed of 300 mm/min and powder feed rate of 17 mg/s) [275]

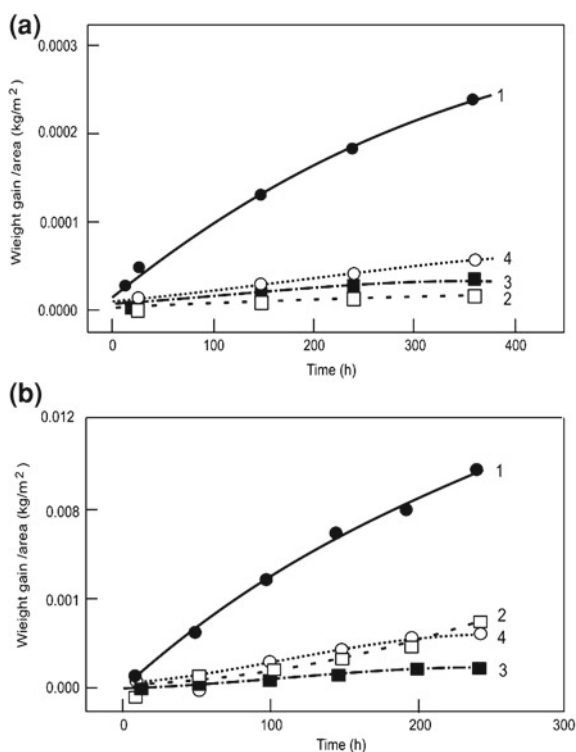


oxidation, the effect of laser surface alloying of Ti with Si or Si + Al on wear resistance was also studied. Under comparable conditions of scratching, Ti undergoes the most rapid wear loss followed by that in laser surface alloyed specimens. The laser alloyed sample with Si undergoes the minimum wear loss. The improved wear resistance of laser surface alloyed Ti with Si was attributed to the formation of a hard Ti_5Si_3 precipitates in the alloyed zone [273].

Manna et al. [276] made an attempt to develop an alternative electrode material for neural stimulation electrode by laser surface alloying of Ti with Ir that can mimic the normal spatiotemporal pattern of neuronal activation by reversible charge transfer. Laser surface alloying was also attempted on magnesium and its alloys to improve wear and corrosion resistance properties. Wang and Wue [277] have achieved significant improvement in corrosion resistance of SiC dispersed Mg by LSC with Al-12Si alloy layer. Ignat et al. [288] studied the effect of laser surface alloying on surface alloying of WE43 and ZE41 Mg alloy with Al using a 3 kW continuous wave Nd:YAG laser and found that the alloyed zone microstructure consisted of Al_3Mg_2 and $\text{Al}_{12}\text{Mg}_{17}$ intermetallics with an improved microhardness and corrosion property.

Similar investigations of laser surface alloying of MEZ with Al + Mn (in 3:1 and 1:1 by weight) using a continuous wave CO_2 laser significantly improved the wear and corrosion properties of the base alloy [279].

Fig. 1.26 Kinetics of isothermal oxidation in terms of weight gain per unit area for as-received Ti (plot 1) and laser surface alloyed Ti with Si (plot 2), 3Si + Al (plot 3), and Si + 3Al (plot 4) [274]



1.9.4 Laser Composite Surfacing

Metal matrix composites generally possess an enhanced wear resistance than the base substrate or the matrix. Although reinforcement of the dispersoid enhances mechanical properties, the degree of reinforcement cannot be unlimited as excessive amount of reinforcement reduces the toughness. Development of composite layer on the surface by conventional means is extremely difficult.

Laser melting of substrate and subsequent feeding of ceramic particles into the molten matrix is an effective means of developing composite layer on the surface through a process called laser composite surfacing. Several attempts have been made to develop a composite layer on metallic matrix by this technique. Cheng et al. [280] have added a mixture of WC–Cr₃C₂–SiC–TiC–CrB₂ and Cr₂O₃ to produce a metal matrix composite surface on stainless steel UNS-S31603. Following laser surface melting, cavitation erosion resistance improved in all cases except for Cr₂O₃. Wu and Hong [281] have attributed the improvement in hardness and corrosion/wear resistance of stainless steel to the presence of amorphous phase in the Zr-rich surface (with 7.8–14.5 wt. % Zr) following laser surface alloying of stainless steel with Zr nanoparticles. Agarwal and Dahotre [282] have reported a substantial improvement in resistance to adhesive/abrasive wear of steel following laser surface alloying with

TiB₂. The surface composite layer containing about 69 vol. % TiB₂ particles recorded an elastic modulus of 477.3 GPa. Similar improvement in wear resistance of mild steel was reported by Tondur et al. [283] due to formation of a FeCr + TiC composite coating formed by laser assisted self-propagating high temperature synthesis. Earlier, Zhukov et al. [284] achieved a similar carbide dispersed composite coating on steel by laser-assisted self-propagating high temperature synthesis. Improvement in hardness and wear resistance has been achieved by laser surface alloying of ferritic steel with Cr₃C₂ + SiC [285]. Development of in situ boride (TiB₂) dispersed composite layer on the surface of AISI 304 stainless steel substrate was achieved with an improved wear resistance [286].

1.9.5 Laser Shock Processing

Laser shock processing involves rapid irradiation of the component surface with a laser (at a power density of $\sim 10^{12}$ W/m²) resulting in generation of shock wave (due to a volume expansion of the plasma plume formed on the surface) and subsequent alteration of microstructure/state of stress. The effect of shock wave may be enhanced when it is propagated through water. This novel laser processing has the capability to improve material hardness and fatigue strength in a number of alloys [287]. The effects of laser shock processing (with a Nd:glass phosphate laser with a 600 ps pulse-width and up to 120 J pulse energy at power densities above 10^{16} W/m²) on the microstructure, microhardness, and residual stress of low carbon steel were studied by Chu et al. [287]. Surface hardness increased up to 80% after the laser shock processing up to 100 μ m in depth and introduced residual compressive stress on the surface. The strengthening effect was attributed to the presence of a high dislocation density.

Peyre et al. [288] showed that laser shock processing offered a better pitting corrosion behavior of AISI 316L stainless steel than that obtained by shot peening in saline environment. Low residual stress and work hardening levels were observed, when compared to that obtained by conventional shot-peening treatment, mainly because of the absence of martensitic transformation in the case of laser processing.

1.9.6 Laser Surface Engineering of Ceramics

Lawrence and Li [289] glazed the surface of Al₂O₃-based refractory by means of high power diode laser and augmented the wear rate and wear life characteristics within both normal and corrosive (NaOH and HNO₃) environmental conditions. Life assessment testing revealed that diode laser generated glaze increased the wear life of the Al₂O₃-based refractory by 1.2–13.4 times depending upon the environmental conditions. Such improvements are attributed to the fact that the microstructure of the Al₂O₃-based refractory was altered from a porous, randomly ordered structure

to a much more dense and consolidated structure after laser treatment that contained fewer cracks and porosities.

Sciti et al. [290] surface treated alumina and silicon carbide ceramics with a KrF excimer laser and studied the influence of laser fluence (1.8 and 7.5 J/cm^2), number of laser pulses (1 – 500), frequency (1 – 120 Hz), pulse duration (25 ns) and shrouding environment on the characteristics of the treated surface. Microstructural analyses of surface and cross-section of the laser processed samples at low fluence (1.8 J/cm^2) evidenced that the surface of both ceramics is covered by a scale due to melting/resolidification. At high fluence (7.5 J/cm^2), there are no continuous scales on the surfaces as material is removed by decomposition/vaporization. On alumina surface, a network of microcracks formed, while on silicon carbide, products of different morphologies (flat and rugged areas, deposits of debris and discontinuous thin remelted scales) were detected.

Schmidt and Li [291] studied the influence of laser glazing of sintered alumina as well as alumina–silica mixtures on surface characteristics and service life using a high power diode laser and high speed motion analysis system for use in a multitude of applications as insulators, crucibles, vacuum system windows, etc. The laser glazed material seems robust and exhibits good adherence to the bulk ceramic.

Stoltz and Poprawe [292] modified the surface conductivity of dielectric ceramics by continuous wave and pulsed laser irradiation. Conductive structures on Al_2O_3 was developed with CO_2 laser and on AlN with excimer laser irradiation (pulse width = 25 ns). Laser-treated specimens were subjected to a detailed characterization of electrical resistivity, chemical composition, structure and morphology.

Polycrystalline ceramics, notably alumina (polycrystalline aluminum oxide) are used widely in the electronics industry as substrates for metal-film deposition, as well as in other industrial applications. Multishot pulsed XeCl excimer laser irradiation of commercial fine-grained polycrystalline alumina substrates is found to significantly improve the bonding characteristics between the metal and film [293]. Laser irradiation produces a smoother surface finish increasing the adhesion strength of subsequently deposited copper films to the laser-treated alumina surface by a factor of 3 – 5 under optimum lasing conditions. X-ray photoelectron spectroscopy measurements suggest that electrical activation of the near-surface region may also contribute to the enhanced copper adhesion.

1.9.7 Laser Surface Engineering of Polymers

Laser-induced surface modification and laser-induced patterning of polymeric surfaces by deposition, etching and ablation has drawn considerable attention of late. Wong et al. [294] irradiated the surface of polyethylene terephthalate with KrF excimer laser (having a wavelength of 248 nm) and studied the surface image using atomic force microscopy. The surface roughness and ripple spacing increased with laser energy. Merging of the ripples (due to surface tension forces) is the driving force for the increased ripple spacing. With appropriate laser treatment, the hydrophobicity

of polyester can be greatly enhanced, making the treated polyester highly unwettable. This provides the textile industry a new method for making a high tech water repellent textile product. Adhi et al. [295] irradiated the surface of polytetrafluoroethylene films by femtosecond UV radiation from an excimer laser (KrF: λ : 248 nm, t_p : 380 fs) in air and investigated the surface using X-ray photoelectron spectroscopy, and bulk by fourier transform infrared spectroscopy. There was no signature of incorporation of hydrogen and/or oxygen, or the formation of a cross-linked network of carbon indicating chemically clean processing in contrast to nanosecond excimer laser processing which chemically degrades the surface. Huang et al. [296] discussed a method of improving adhesion to fluorocarbon resin by irradiation with an XeCl excimer laser. The respective adhesive force between the polymer and metal, and contact angles with water was measured by the shear test method and an Ne–He laser system. The adhesive force improved when the polymer surface was irradiated in the presence of water or solutions of boric acid, sodium hydroxide, copper sulfate, and sodium aluminate. These results were interpreted in terms of a simple laser heating model.

Drinek et al. [297] photolyzed hexamethylcyclotrisilazane (HMCTS) at 84 K using ArF excimer laser and film changed into a polymer having siloxane units in air at room temperature. However, fragments generated by laser irradiation of this polymer in the frozen film made a similar polymer film having a siloxane structure on a PVA film in air. The polymeric film with siloxane units prepared by the cryogenic laser ablation method displayed hydrophobic properties. Lu et al. [298] surface modified polyimide film by pulsed ultraviolet (UV) laser. Irradiation caused a photochemical reaction in the hydrophilic groups. In addition, a ripple microstructure was formed on the suz laser beam was 20 – 50°. Csete and Bor [299] generated laser-induced periodic surface structures on oriented and amorphous thick, as well as on spin-coated thin, polycarbonate films by polarized ArF excimer laser. Studies on the influence of the film structure and thickness on the development of periodic surface structure revealed that the line-shaped structure would transform into droplets below a critical thickness of the spin-coated films. This droplet formation was explained by the laser-induced melting across the film and subsequent dewetting on the substrate. The thickness of the layer melted by laser irradiation was computed by a heat conduction model, compared well with the critical thickness for spin-coated film. Hartwig [300] studied the influence of eximer laser radiation (248 nm) on the surface properties of an epoxy resin. At low laser energy density, the lap shear strength with the epoxy based adhesive was on an appropriate level with an improved reproducibility, but at higher energy densities the lap shear strength decreased due to the decomposition of the resin surface, as revealed by X-ray photoelectron spectroscopy results. Frerichs et al. [301] conducted a detailed investigation on laser ablation of different polymers like polyamide, polystyrene, polycarbonate, and polypropylene using a 248 nm excimer laser to study the effect of laser parameters on surface structuring. Arenholz et al. [302] showed that the adhesion of metal films on polymer foils could be improved by laser irradiation of the polymer surface prior to metal deposition. As a model system, metal films of different Co alloys, such as CoNi, CoCr, and CoNi-oxide, were chosen to form deposits on polytetraethylene foils. Laser irradiation was performed by means of a 248 nm KrF and 308 nm XeCl laser light in

1 – 20 pulses with fluences of typically 5 mJ/cm^2 and 40 mJ/cm^2 , respectively. Post irradiation metal deposition was carried out by electron-beam evaporation immediately after laser-beam irradiation. Laser irradiation of untreated poly-tetra-ethylene foils resulted in the formation of wall-type or map-type structures the mean distance of which was found to be related to laser parameters.

Different methods of laser treatment are suitable to generate grating-like periodic structures on polymer surfaces. One possibility is the projection of a mask and realization of periodic ablation [303]. The resulting periodicity is limited by the resolution of the applied optical system and by the complex response of the material to the laser illumination [304]. This method is suitable for generating structures in the micrometer-size region without difficulty. Smaller structures can be induced in the near field of the grating by the Talbot effect [305, 306].

1.10 Summary and Future Scope

Laser assisted fabrication offers a range of direct or single-step, contact-less and novel method of fabricating finished products/components of metallic, ceramic and polymeric origin. The possibilities offered by laser-assisted fabrication include bending, rapid prototyping, direct manufacturing, machining, welding, and surface engineering. Laser bending is attractive to the automobile and aircraft industry both for the precision and productivity involved in the process. Laser bending that primarily depends upon ‘temperature gradient’ and ‘buckling’ mechanisms is routinely applied in tailoring the curvature of aluminum, iron, and titanium-based metals and alloys. Laser assisted manufacturing is a major laser forming process that has found commercialization in many applications. The main reasons for interest in this process stems from the scope of direct (one-step) manufacturing of round or square sections, hollow tubes, and more complex geometry with the same machine and identical fixture. Solid parts are usually made in layers. Thus, the interfaces of the consecutive layers remain the weakest point. Investigations are warranted to predict the stresses generated at the edges and corners, surface roughness/contour, and compositional distribution in the solid object. Development or epitaxial repair of single crystal superalloy component will be a real breakthrough. In this regard, more comprehensive treatments of heat and mass transfer in specific applications are warranted to establish the reproducibility of the laser forming processes.

Laser machining requires controlled removal of material by vaporizing within a narrow dimension incurring least heating of the surrounding. The process can be extended to cutting, drilling, scribing, marking, or cleaning. In all these processes, material removal without damaging the surrounding and maintaining precision and accuracy is a challenge. The recent advances are now based on selecting appropriate wavelength, using multiple beams, allowing inclined/oblique incidence and removing material in stages. A large variety of materials starting from human/animal tissues to diamond can be laser machined. However, an appropriate choice of laser power and wavelength is crucial for the success of the operation. Future challenges

include increasing the capability to machine thicker sections, curved surfaces, and dissimilar/heterogeneous materials. Similarly, assessment of material damage needs more close control and monitoring of the microstructural change/damage across the cut. Development of intelligent machines for machining diverse materials would require interfacing a vast database with the hardware. Thus, continued efforts are needed to model laser machining processes with suitable experimental validation of the predicted results.

1.11 Future Challenges

This article has presented an overview of the fundamentals of laser, laser–matter interaction, and application of laser with regard to material processing divided into four major categories, namely forming, joining, machining, and surface engineering. Although lasers were invented in the early twentieth century, commercial high power lasers capable of delivering adequate power density for material processing involving heating, melting, and vaporising from all engineering solids (metallic, ceramic, semi-conducting, polymeric, and composites) were developed nearly 40 years ago and the application of laser in materials fabrication became popular only in the 1980s and onwards. The challenges in this regard lie in the development of novel and nonequilibrium microstructure including amorphous and extended solid solutions by ultrarapid cooling developed by laser melting and associated rapid solidification. Although attempts were made in developing amorphous/bulk metallic glass structure by laser surface cladding, complete amorphization could not be achieved due to the presence of heterogeneous nucleation sites at the solid–liquid interface and successive annealing of the zone during laser processing by successive laser passes. Hence, extensive efforts need to be undertaken in the development of a laser system for this purpose and designing of experiments in this regard.

The extensive amount of literature reviewed in this article clearly suggests that the field is far from being saturated and is rather rapidly growing into new and unexplored areas of application. The biggest advantage of laser is its ability to be a contact-less heating tool that can deliver the desired quantum of thermal energy in all solids at a precise location irrespective of their chemical bonding/nature, physical dimension (small or big), and state of aggregate (pure, mixed, composite) with minimum damages to the surrounding. Although the laser-induced heating or thermal profile decays exponentially with depth, the possibility of coupling laser with modern engineering practices like computer-aided design and manufacturing using robot-controlled stage and pneumatic/mechanically-driven delivery system (of wire, powder, sheet) has enabled creation of large components practically of any desired dimension and geometry. The versatility is further extended in the ability of laser to simultaneously heat, add, join, or remove materials of dissimilar nature like conducting and nonconducting, hard and soft, and dense and porous. Laser is now utilized to close surface porosities on coated and welded products and also for creating graded aggregate with controlled porosity, composition, and microstructure. This microstructural or

compositional gradation can be achieved within very narrow to wide length scales and along horizontal or vertical directions.

Acknowledgements The authors gratefully acknowledge the continuous supports from Prof. W. M. Steen, Prof. K. G. Watkins; Prof. A. K. Nath, Prof. B. L. Mordike, Dr. Andreas Weisheit, Dr. Rolf Galun, Prof. Lin Li for extending their laser facilities for research work and scientific collaboration. Experimental results presented in this chapter were mostly performed by their students: Dr. B. Ramesh Chandra, Dr. A. Basu, Dr. A. Biswas, Dr. S. Chatterjee, Mr. Subhasisa Nath and Mr. Prashant Sharma. Financial assistance from German Academic Exchange Service (DAAD), N. Delhi; Department of Science and Technology (DST), New Delhi; Council of Scientific and Industrial Research (CSIR); New Delhi; Board of Research on Nuclear Science (BRNS), and Bombay and Naval Research Board (NRB); New Delhi are gratefully acknowledged.

References

1. J.F. Ready, D.F. Farson, T. Feeley, *LIA Handbook of Laser Materials Processing* (Springer, Berlin, 2001) pp. 1.
2. W.M. Steen, K. Watkins, *Laser Material Processing* (Springer, New York, 2003) pp. 1.
3. B.L. Mordike, *Materials Science and Technology*, vol. 15, eds. by R.W. Cahn, P. Haasen, E.J. Kramer (VCH, Weinheim, 1993), p. 111
4. J. Mazumdar, *Lasers for Materials Processing*, ed. by M. Bass (North Holland Pub. Co., New York, 1993), p. 113
5. N.N. Rykalin, A. Uglov, A. Kokora, *Laser Machining and Welding* (MIR, Moscow, 1978), p. 1
6. S.T. Picraux, D.M. Follstaedt, *Laser-Solid Interactions and Transient Thermal Processing of Materials*, eds. by J. Narayan, W.L. Brown, R.A. Lemons (North-Holland Pub. Co., New York, 1983), p. 751
7. A. Einstein, *Z. Phys.* **18**, 121–128 (1917)
8. H. Kopfermann, R. Ladenburg, *H. Phys. Chemie. Abt.* **139**, 375–385 (1928)
9. T.H. Maiman, *Nature* **187**, 493–494 (1960)
10. O. Svelto, *Principles of Lasers* (Plenum Press, New York, 1986) pp. 1.
11. M.I. Nathan, W.P. Dumke, G. Burns, F.H. Dill Jr, *J. Appl. Phys. Lett* **1**, 62–64 (1962)
12. R.N. Hall, G.E. Fenner, J.D. Kingsley, T.J. Soltya, R.O. Carlson, *Phys. Rev. Lett* **9**, 366–368 (1962)
13. M.H.R. Hutchinson, *Spectrochim. Acta—Part B* **58**, 1155–1161 (2003)
14. G. Bekefi, *Principles of Lasers Plasmas* (New York, Wiley, 1976) pp. 1.
15. G. Patrick, O. ÓShea, P. Henry, *Science* **292**, 1853–1858 (2001)
16. M.D. Perry, D. Pennington, B.C. Stuart, G. Tietbohl, J.A. Britten, C. Brown, S. Herman, B. Golick, M. Kartz, J. Miller, H.T. Powell, M. Vergino, V. Yanovsky, *Opt. Lett.* **24**, 160–162 (1999)
17. Y. Kitagawa, Y. Sentoku, S. Akamatsu, M. Mori, Y. Tohyama, R. Kodama, K.A. Tanaka, H. Fujita, H. Yoshida, S. Matsuo, T. Jitsuno, T. Kawasaki, S. Sakabe, H. Nishimura, Y. Izawa, K. Mima, T. Yamanaka, *Plasmas* **9**, 2202–2207 (2002)
18. C.W. White, M.J. Aziz, *Surface Alloying by Ion, Electron and Laser Beams*, eds. by L.E. Rehn, S.T. Picraux, H. Wiedersich, (ASM, Metals Park, Ohio, 1987), p. 19
19. S. Lugomer, G. Bitelli, *Vacuum* **47**, 13–22 (1996)
20. J.H. Chu, J.-B. Du, I. Lin, *J. Appl. Phys. D* **27**, 296–300 (1994)
21. J.H. Chu, I. Lin, *Physica* **205**, 183–190 (1994)
22. A. Melzer, T. Trottenberg, A. Piel, *Phys. Lett. A.* **191**, 301–308 (1994)

23. A. Piel, A. Melzer, *Adv. Space. Res.* **29**, 1255–1264 (2002)
24. A.G. Gnedovets, E.B. Kul'batskii, I. Smurov, G. Flamant, *Appl. Surf. Sci.* **96**(98), 272–279 (1996)
25. R. Cauble, P.M. Celliers, G.W. Collins, L.B. da Silva, D.M. Gold, M.E. Foord, K.S. Budil, R.J. Wallace, A. Ng, *J. Suppl. Ser.* **127**, 267–273 (2000)
26. G.W. Collins, P.M. Celliers, L.B. DaSilva, R. Cauble, D.M. Gold, M.E. Foord, N.C. Holmes, B.A. Hammel, R.J. Wallace, A. Ng: *Phys. Rev. Lett.* **87**(16), art. no. 165504 (2001)
27. J. Laeng, J.G. Stewart, F.W. Liou, *Inter. J. Prod. Res.* **38**, 3973–3996 (2000)
28. Y. Namba, in *Proceedings International Conference of Lasers and Electro-Optics (ICALEO '85)*, Laser Institute of America, Orlando, Boston, MA, Sept 1985, pp. 403–407
29. Y. Namba, in *Proceedings Laser Advanced Materials Processing (LAMP '87)*, High Temperature Society of Japan, Osaka, Japan, June 1987, pp. 601–606
30. F. Vollersten, in *Laser Assisted Net Shape Engineering Meisenbach, Mechanisms and models for laser forming*, eds. by M. Geiger, F. Vollersten, (Bamberg, 1994), pp. 345–360
31. F. Vollersten, M. Rödle, in *Laser Assisted Net Shape Engineering Meisenbach, Model for the temperature gradient mechanism in laser bending*, eds. by M. Geiger, F. Vollersten, (Bamberg, 1994) pp. 371–378
32. F. Vollersten, S. Holzer, *VDI-Z.* **136**, 35–38 (1994)
33. M. Geiger, F. Vollersten, *Ann CIRP.* **42**, 301–304 (1993)
34. H. Arnet, F. Vollertsen, *J. Eng. Manuf.* **209**, 433–442 (1995)
35. F. Vollersten, I. Komel, R. Kals, *Mater. Sci. Eng.* **3**, 107–119 (1995)
36. Y. Li, N.R. Quick, A. Kar, *J. Mater. Proc. Technol.* **123**, 451–458 (2002)
37. M. Geiger, *Synergy Laser Mater. Process. Technol.* **120**, 322–326 (2002)
38. D. Chen, S. Wu, M. Li, *J. Mater. Proc. Technol.* **148**, 30–34 (2004)
39. M. Marya, G.R. Edwards, *J. Mater. Process. Technol.* **108**, 376–383 (2001)
40. P.J. Cheng, S.C. Lin, *J. Mater. Proc. Technol.* **108**, 314–319 (2001)
41. R. Kovacevic, Z. Hu, M. Labudovic, H. Wang, *Int. J. Mach. Tools Manuf.* **41**, 589–607 (2001)
42. C. Peng, Y.Y. Lawrence, *J. Manuf. Sci. Eng. (Trans. ASME).* **127**, 572–582 (2005)
43. W. Shichun, Z. Jinsong, *J. Mater. Proc. Technol.* **110**, 160–163 (2001)
44. J. Lawrence, M.J.J. Schmidt, L. Li, *Int. J. Mach. Tools and Manu.* **41**, 967–977 (2001)
45. S. Yoshioka, T. Miyazaki, M. Imai, Y. Shirai, T. Misu, in *Proceedings Conference on Laser Materials Processing*, ICALEO '98, Orlando, Florida, Nov 1998, Section E, pp. 161–169.
46. J. Dutta Majumdar, A.K. Nath, I. Manna, *Mater. Sci. Engg.* **385**, 113–122 (2004)
47. X.F. Wang, J. Takacs, G. Krallics, A. Szilagyi, T. Markovits, *J. Mater. Process. Technol.* **127**, 388–391 (2002)
48. W. Li, Y.L. Yao, *Trans. ASME* **123**, 674–681 (2001)
49. K.C. Chan, J. Liang, *Mater. Lett.* **49**, 51–55 (2001)
50. J. Magee, K.G. Watkins, W.M. Steen, N.J. calder J. Sidhu, J. Kirby, in *Conference ICALEO '97, Laser Materials Processing*, Vol. 83. II, San Diego, California, USA, 17–20 Nov 1997, pp. E156–E165
51. J. Magee, K.G. Watkins, W.M. Steen, R.L. Cooke, J. Sidhu, *Conference, ICALEO '98, Laser Materials Processing*, Orlando, Florida, Section E, 16–19 Nov 1998, pp. 141–150
52. J. Magee, J. Sidhu, R.L. Cooke, *Opt. Lasers Eng.* **34**, 339–353 (2000)
53. R.J. Blake, in *Conference, ICALEO '96, Laser Materials Processing*, Detroit, Michigan, USA, 14–17 Oct 1996, pp. E105–E114
54. R.J. Blake, R.M. Pearson, A.B. Royell, W.E. Simon, *J. Laser Appl.* **10**, 199–204 (1998)
55. W. Maher, K.O. Tong, C. Bampton, M. Bright, J. Wooten, C. Rhodes, in *Conference, ICALEO '98, Laser Materials Processing*, Orlando, Florida, 16–19 Nov 1998, pp. 141–150.
56. T. Hatayama, M. Osawa, Netsu Shori (J. Jpn. Soc. Heat Treat.) **40**, 116–121 (2000)
57. K. Okuda, S. Shimoyama, M. Nunobiki, *Key Engg. Mater.* **257–258**, 541–546 (2004)
58. K.C. Chan, Y. Harada, J. Liang, F. Yoshida, *J. Mater. Proc. Tech.* **122**, 272–277 (2002)
59. F.R. Liu, K.C. Chan, C.Y. Tang, *Mater. Sci. Eng. A.* **396**, 172–180 (2005)

60. J.A. Ramos, J. Magee, K.G. Watkins, W.M. Steen, F. Noble, in *Conference, ICALEO '98, Laser Materials Processing*, Orlando, Florida, 16–19 Nov 1998, Section E, pp. 178–185
61. M. Marya, G.R. Edwards, in *5th International Conference on Trends in Welding Research*, Pine Mountain, GA, USA, 1–5 June 1998, pp. 982–987. Florida, Section E, 16–19 Nov 1998 pp. 121–130
62. W. Wiehua-Wang, M.R. Holl, D.T. Schwartz, J. Electrochem. Soc. **148**, 363–368 (2001)
63. A. Greco, A. Licciulli, A. Maffezzoli, J. Mater. Sci. **36**, 99–105 (2001)
64. L. Lu, J.Y.H. Fuh, Z.D. Chen, C.C. Leong, Y.S. Wong, Mater. Res. Bull. **35**, 1555–1561 (2000)
65. K. Daneshvar, M. Raissi, S.M. Bobbio, J. Appl. Phys. **88**, 2205–2210 (2000)
66. M.C. Wanke, O. Lehmann, K. Muller, W. Qingzhe, M. Stuke, Science. **275**, 1284–1286 (1997)
67. O. Lehmann, M. Stuke, Science **270**, 1644–1646 (1995)
68. M. Burns, *Automotive Fabrication: Improving Productivity in Manufacturing*, (PTR Prentice-Hall Inc., Englewood Cliffs, 1993)
69. B.K. Paul, S. Baskaran, J. Mater. Process. Technol. **61**, 168–172 (1996)
70. D. Kochan, *Solid Freeform Manufacturing* (Elsevier, Amsterdam, 1993)
71. J. Pacheco, *Rapid Prototyping*, Contract no. DLA900-90-D-0134, (Department of Defense, Manufacturing Technology Information Analysis Center, Chicago, 1993)
72. M.L. Griffith, J.W. Halloran, in *Proceedings of the Solid Freeform Fabrication Symposium*, eds. by H.L. Marcus et al., (University of Texas, Austin 1994), p. 396
73. M.L. Griffith, T.M. Chu, W.C. Wagner, J.W. Halloran, in *Proceedings of the Solid Freeform Fabrication Symposium*, eds. by H.L. Marcus et al., (University of Texas, Austin, 1995), p. 31
74. R.S. Crockett, J. Okelly, P.D. Calvert, B.D. fabes, K. Stuffle, P. Greegan, R. Hoffman, in *Proceedings of the Solid Freeform fabrication Symposium*, eds. by H.L. Marcus et al., (University of Texas, Austin, 1995), p. 17
75. J.D. Cawley, P. Wei, Z.E. Liu, W.S. Newman, B.B. Mathewson, A. H. Heuer, in *Proceedings of the Solid Freeform fabrication Symposium*, eds. by H.L. Marcus et al., (University of Texas, Austin, 1995), p. 9
76. C. Groffin, J. Daufenbach, S. McMillin, Bull. Am. Ceram. Soc. **73**, 109 (1994)
77. J. Dutta Majumdar, I. Manna, Sadhana **28**, 495–562 (2003)
78. K. Lewis, E. Schlienger, Mater. Design **21**, 417–423 (2000)
79. Y.Z. Zhang, L.K. Shi, J. Cheng, M.Z. Xi, J. Xu, J Adv. Mater **35**, 36–40 (2003)
80. E. Goode, Adv. Mater. Process. **161**, 66–67 (2003)
81. K. Dai, L. Shaw, Acta Materialia. **52**, 69–80 (2004)
82. K. McAlea, C. Nelson, U. Heimadi, S. Seitz, in *Conference on Rapid Prototyping/ Laser Applications in the Automotive Industries*, Florence, Italy, 16–19 June 1997, pp. 159–167
83. A. Bauer, J. Ganz, K. Hesse, E. Kohler, Appl. Surf. Sci. **46**, 113–120 (1990)
84. F. Micheli, I.W. Boyd, Opt. Laser Technol. **18**, 75–82 (1987)
85. M.L. Griffith, M.E. Schlienger, L.D. Harwell, M.S. Oliver, M.D. Baldwin, M.T. Ensz, M. Essien, J. Brooks, C.V. Robino, J.E. Smugeresky, W.H. Hofmeister, M.J. Wert, D.V. Nelson, Mater. Design **20**, 107–113 (1999)
86. J.-Y. Jeng, M.-C. Lin, J. Mater. Process. Technol. **110**, 98–103 (2001)
87. C.L. Kuo, J.D. Huang, H.Y. Liang, Int. J. Adv. Manuf. Technol. **21**, 796–800 (2003)
88. D.S. Choi, S.H. Lee, B.S. Shin, K.H. Whang, Y.A. Song, S.H. Park, H.S. Jee, J. Mater. Proc. Technol. **113**, 273–279 (2001)
89. A.L. Kovalev, V.P. Mishina, D.L. Wainstein, V.I. Titov, V.F. Moiseev, N.K. Tolochko, J. Mater. Eng. Perform. **11**, 492–495 (2002)
90. Y. Tang, H.T. Loh, Y.S. Wong, J.Y.H. Fuh, L. Lu, X. Wang, J. Mater. Proc. Tech. **140**, 368–372 (2003)
91. X.H. Wang, J.Y.H. Fun, Y.S. Wong, L. Lu, H.T. Loh, Y.X. Tang, H.H. Zhu, Mater. Sci. Forum, 437–438, 273–276 (2003)
92. M.W. Khaing, J.Y.H. Fuh, L. Lu, J. mater. Proc. Technol **113**, 269–272 (2001)

93. Y.P. Kathuria, in *Proceedings, 60 Years of Scientific Co-operation in Welding, Jubilee Conference*, Timisoara, 19–21 Nov 1997, pp. 199–205
94. S. Hayano, *Titanium Japan* **50**, 43–47 (2002)
95. N.K. Tolochko, V.V. Savich, T. Laoui, L. Froyen, G. Onofrio, E. Signorelli, V.I. Totov, J. Mater. Design Appl. **216**, 267–270 (2002)
96. J.-Y. Jeng, S.-C. Peng, C.-J. Chou, *Int. J. Adv. Manuf. Technol.* **16**, 681–687 (2000)
97. A.J. Pinkerton, L. Li, *Int. J. Mach. Tools Manuf.* **44**, 573–584 (2004)
98. A.J. Pinkerton, L. Li, *Appl. Surf. Sci.* **208–209**, 405–416 (2003)
99. J. Dutta Majumdar, A. Pinkerton, Z. Liu, I. Manna, L. Li, *Appl. Surf. Sci.* **247**, 320–327 (2005)
100. J. Dutta Majumdar, A. Pinkerton, Z. Liu, I. Manna, L. Li, *Appl. Surf. Sci.* **247**, 373–377 (2005)
101. G.J. Davies, S. Zhen, *J. Mater. Sci.* **18**, 1899–1902 (1983)
102. Y.P. Kathuria, *J. Mater. Proc. Technol.* **142**, 466–470 (2003)
103. Y. Zhang, M. Xi, S. Gao, L. Shi, *J. Mater. Proc. Technol.* **142**, 582–585 (2003)
104. J. Mei, J. Liang, R. Sharman, W. Voice, X. Xu, in *Conference on Rapid Prototyping of Materials*, Columbus, 7–10 Oct 2002, pp. 133–138
105. F.G. Arcella, F.H. Froes, *JOM* **52**, 28–30 (2000)
106. D.H. Abbott, F.G. Arcella, *Adv. Mater. Proc.* **153**, 29–30 (1998)
107. D. Srivastava, I.T.H. Chang, M.H. Loretto, *Mater. Design* **21**, 425–433 (2000)
108. D. Srivastava, I.T.H. Chang, M.H. Loretto, *Intermetallics* **9**, 1003–1013 (2001)
109. R. Banerjee, P.C. Collins, A. Gene, H.L. Fraser, *Mater. Sci. Eng. A* **358**, 343–349 (2003)
110. R. Banerjee, P.C. Collins, D.C. Bhattacharyya, S. Banerjee, H.L. Fraser, *Acta Materialia* **51**, 3277–3292 (2003)
111. R. Banerjee, P.C. Collins, H.L. Fraser, *Adv. Engg. Mater. (Germany)* **4**, 847–851 (2002)
112. H. Tomochika, H. Kikuchi, T. Araki, M. Nishida, *Mater. Sci. Eng. A* **356**, 122–129 (2003)
113. X.D. Zhang, C. Brice, D.W. Mahaffey, H. Zhang, K. Schwendner, D.J. Evans, H.L. Fraser, *Scripta Materialia* **44**, 2419–2424 (2001)
114. X. Wu, J. Mei, *J. Mater. Process. Technol.* **135**, 266–270 (2003)
115. Y.X. Tang, L. Lu, Y.H.J. Euh, H.T. Loh, Y.S. Wong, C.H. Ng, *Mater. Sci. Forum* **437**(438), 301–304 (2003)
116. W.L. Karlsen, J. Kotila, J.E. Lind, *Int. J. Powder Metall.* **40**, 29–41 (2004)
117. L. Xue, J.Y. Chen, M.U. Islam, in *Conference on Laser Materials Processing, ICALEO 1999*, San Diego, 15–18 Nov 1999
118. S. Das, T.P. Fuesting, G. Danyo, L.E. Brown, J.J. Beaman, D.L. Bourell, *Mater. Design* **21**, 63–73 (2000)
119. K. Cai, D. Guo, Y. Huang, J. Yang, *J. Eur. Ceram. Soc.* **23**, 921–925 (2003)
120. A. Larrea, de la G.F. Fuente, R.I. Merino, V.M. Orera, *J. Eur. Ceram. Soc.* **22**, 191–198 (2002)
121. L. Lu, J.Y.H. Fuh, Z.D. Chen, C.C. Leong, Y.S. Wong, *Mater. Res. Bull.* **35**, 1555–1561 (2000)
122. W. Liu, J.N. DuPont, *Scripta Materialia* **48**, 1337–1342 (2003)
123. Y.P. Kathuria, *Surf. Coat. Technol.* **116–119**, 643–647 (1999)
124. H.M. Wang, D.Y. Luan, L.Y. Zhang, *Scripta Materialia* **48**, 1179–1184 (2003)
125. G. Duan, H.M. Wang, *J. Mater. Sci. (U.S.A.)* **37**, 1981–1985 (2002)
126. J. Cheng, Y.Z. Zhang, P.Z. Zhang, L.K. Shi, M.Z. Xi, *Heat Treat. Met. (China)* **3**, 32–35 (2002)
127. J. Bosbach, D. Martin, F. Stietz, T. Wenzel, F. Träger, *Appl. Phys. Lett.* **74**, 2605–2608 (1999)
128. M.C. Wanke, O. Lehmann, K. Muller, W. Qingzhe, M. Stuke, *Science. Assoc. Adv. Sci.* **275**, 1284–1286 (1997)
129. Y.F. Lu, H. Qiu, *J. Appl. Phys.* **88**, 1082–1087 (2000)
130. S. Fukumoto, A. Hirose, K.F. Kobayashi, *Mater. Sci. Technol.* **9**, 264–271 (1993)
131. C.A. Forbis-Parrott, *Weld. J.* **70**, 37–42 (1991)
132. S.T. Riches, *Weld. Met. Fabr.* **61**, 79–83 (1993)
133. R.S. Parmar, *Welding Engineering and Technology* (Khanna Publishers, New Delhi, 1999)
134. J. F. Lancaster, *Metallurgy of Welding* (George Allen and Unwin, 1980)

135. W.W. Duley (eds.), *Laser Welding* (Wiley, New York, 1999) pp. 1.
136. K.H. Leong, P.A. Kirkham, K.C. Meinert Jr., *J. Laser Appl.* **12**, 181–184 (2000)
137. A. Hirose, H. Todaka, K. Yamaoka, N. Kurosawa, K.F. Kobayashi, *Metall. Mater. Trans. A* **30**, 2115–2120 (1999)
138. D.C. Weckman, H.W. Kerr, J.T. Liu, *Metall. Mater. Trans. B* **28**, 687–700 (1997)
139. M.F. Lee, J.C. Huang, N.J. Ho, *J. Mater. Sci.* **31**, 1455–1468 (1996)
140. I.R. Whitaker, D.G. McCartney, *Mater. Sci. Eng. A* **196**, 155–163 (1995)
141. E. Biro, Y. Zhou, D.C. Weckman, K.J. Ely, *J. Laser Appl.* **13**, 96–104 (2001)
142. T. Fuhrich, P. Berger, H.J. Hugel, *J. Laser Appl.* **13**, 178–186 (2001)
143. M. Farid, P.A. Molian, *J. Mater. Sci.* **15**, 3817–3826 (2000)
144. E.S. Ng, I.A. Watson, *J. Laser Appl.* **11**, 273–278 (1999)
145. A.M. El-Batahy, *Mater. Lett.* **32**, 155–163 (1997)
146. Z. Szymanski, J. Kurzyrna, W. Kalita, *J. Phys. D (Appl. Phys.)* **30**, 3153–3162 (1997)
147. Wood-Hi-Cheng, Wei-Han-Wang, Jyh-Cheng-Chen: *IEEE Trans. Compon. Packag. Manuf. Technol.* **19**, 764–769 (1996)
148. G. Wang, K.N. Tandon, *Microgravity Sci. Technol.* **8**, 131–133 (1995)
149. T.T. Hsu, Y.R. Wang, S.K. Wu, C. Chen, *Metall. Mater. Trans. A* **32**, 569–576 (2001)
150. O. Perret, M. Bizouard, Ph. Naudy, G. Pascal, D. Nore, Y. Horde, Y. Delaisse, *J. Appl. Phys.* **90**, 27–30 (2001)
151. L.W. Tsay, C.Y. Tsay, *Inter. J. Fatigue* **19**, 713–720 (1997)
152. A. Hirose, S. Fukumoto, K.F. Kobayashi, *Key Eng. Mater.* **104–107**, 853–872 (1995)
153. M. Marya, G.R. Edwards, *J. Mater. Eng. Perform.* **4**, 435–443 (2001)
154. T. Shida, M. Hirokawa, S. Sato, *Weld. Res. Abroad* **43**, 36 (1997)
155. E.L. Baarden, D.J. Schmatz, R.E. Bisaro, *Weld. J.* **52**, 227 (1973)
156. R.A. Willgoss, J.H.P.C. Megaw, J.N. Clark, *Opt. Laser Technol.* **11**, 73 (1979)
157. R. C. Crafer, in *Proceedings of 4th International Conference on Advances in Welding Processes*, Harrogate, Yorks, 9–11 May 1978, pp. 267–278
158. J. Majumdar, W.M. Steen, *Met. Trans. A* **13**, 865 (1982)
159. Y.S. Yang, S.H. Lee, *J. Mater. Process. Technol.* **94**, 151–156 (1999)
160. C.M. Banas, *Laser Welding Developments*, in *Proceedings GECB International Conference on Welding Research Related to Power Plants*, 17–21 Sept 1972, Southampton, England
161. B.G. Chung, S. Rhee, C.H. Lee, *Mater. Sci. Eng. A* **272**, 357–362 (1999)
162. F. Malek Ghaini, M.J. Hamed, M.J. Torkamany, J. Sabbaghzadeh, *Scripta Materialia* **56**, 955–958 (2007)
163. C.T. Kwok, S.L. Fong, F.T. Cheng, H.C. Man, *J. Mater. Process. Technol.* **176**, 168–178 (2006)
164. N.A. McPherson, K. Chi, T.N. Baker, *J. Mater. Proc. Technol.* **134**, 174–179 (2003)
165. A.-M. El-Batahy, *Mater. Lett.* **32** (1997) 155–163
166. S.M. Chan, L.C. Chan, T.C. Lee, *J. Mater. Process. Technol.* **132**, 95–101 (2003)
167. Z. Sun, M. Kuo, T. Moisio, *J. Mater. Sci. Lett.* **17**, 355–357 (1998)
168. A.P. Costa, L. Quintino, M. Greitmann, *J. Mater. Process. Technol.* **141**, 163–173 (2003)
169. R. Akhter, K.G. Watkins, W.M. Steen, *Mater. Lett.* **9**, 550–556 (1990)
170. S. Iqbal, M.M.S. Gualini, F. Grassi, *J. Mater. Process. Technol.* **184**, 12–18 (2007)
171. L.W. Tsay, M.C. Young, C. Chen, *Corr. Sci.* **45**, 1985–1997 (2003)
172. E. Capello, P. Chiarello, B. Previtali, M. Vedani, *Mater. Sci. Engg. A* **351**, 334–343 (2003)
173. W.S. Chang, S.J. Na, *J. Mater. Proc. Technol.* **120**, 208–214 (2002)
174. Y.-F. Tzeng, *J. Mater. Process. Technol.* **102**, 40–47 (2000)
175. Z. Li, G. Fontana, *J. Mater. Proc. Technol.* **74**, 174–182 (1998)
176. T. Narikiyo, H. Miura, S. Fujinaga, A. Ohmori, K. Inoue, *J. Phys. D Appl. Phys.* **31**, 2331–2337 (1998)
177. J. Onoro, C. Ranninger, *J. Mater. Proc. Technol.* **68**, 68–70 (1997)
178. H. Kusuda, T. Takasago, F. Natsumi, *J. Mater. Proc. Tech.* **71**, 136–140 (1997)
179. A. Roustila, N. Kuromoto, A.M. Brass, J. Chene, *J. Nucl. Mater.* **211**, 156–167 (1994)

180. E. Schubert, M. Classen, I. Zerner, C. Walz, G. Sepold, J. Maters. Proc. Technol. **115**, 2–8 (2001)
181. A. Haboudoua, P. Peyrea, A.B. Vannes, G. Peix, Mater. Sci. Eng. A **363**, 40–52 (2003)
182. R. Braun, Mater. Sci. Eng. A **426**, 250–262 (2006)
183. T.M. Yue, J.H. Xu, H.C. Man, Appl. Compos. Mater. **4**, 53–64 (1997)
184. H.M. Wang, Y.L. Chen, L.G. Yu, Mater. Sci. Eng. A **293**, 1–6 (2000)
185. Q. Yunlian, D. Ju, H. Quan, Z. Liying, Mater. Sci. Eng. A **280**, 177–181 (2000)
186. A.P. Wu, G.S. Zou, J.L. Ren, H.J. Zhang, G.Q. Wang, X. Liu, M.R. Xie, Intermetallics **10**, 647–652 (2002)
187. K. Uenishi, K.F. Kobayashi, Intermetallics **4**, 95–101 (1996)
188. Z. Li, S.L. Gobbi, I. Norris, S. Zolotovskiy, K.H. Richter, J. Maters. Proc. Technol. **65**, 203–208 (1997)
189. K. Girard, J.M. Jouvard, Ph. Naudy, J. Phys. D: Appl. Phys. **33**, 2815–2824 (2000)
190. Z. Xu, K. Natesan, C.B. Reed, D.L. Smith, Int. J. Ref. Met. Hard Mater. **18**, 231–236 (2000)
191. L.i. Zhang, S.L. Gobbi, K.H. Richter, J. Maters. Proc. Tech. **70**, 285–292 (1997)
192. G. Song, L. Liu, P. Wang, Mater. Sci. Eng. A **429**, 312–319 (2006)
193. L. Liming, W. Jifeng, S. Gang, Mater. Sci. Eng. A **381**, 129–133 (2004)
194. J.H. Kim, C. Lee, D.M. Lee, J.H. Sun, S.Y. Shin, J.C. Bae, Maters. Sci. Engg. A **449–451**, 872–875 (2007).
195. Y.L. Chen, L.G. Yu, H.M. Wang, Proc. SPIE. **3862**, 443–447 (1999)
196. G. Sierra, P. Peyre, F. Deschaux-Beaume, D. Stuart, G. Fras, Mater. Sci. Eng. A **447** 197–208, (2007)
197. B. Majumdar, R. Galun, A. Weisheit, B.L. Mordike, J. Maters. Sci. **32**, 6191–6200 (1997)
198. T.A. Mai, A.C. Spowage, Mater. Sci. Eng. A **374**, 224–233 (2004)
199. F.L. Chen, E. Siores, J. Mater. Proc. Technol. **141**, 213–218 (2003)
200. P. Di Pietro, Y.L. Yao, Int. J. Mach. Tools Manuf. **35**, 673–688 (1995)
201. J. Duan, H.C. Man, T.M. Yue, J. Phys D: Appl. Phys. **34**, 2127–2134 (2001)
202. J. Duan, H.C. Man, T.M. Yue, J. Phys. D: Appl. Phys. **34**, 2135–2142 (2001)
203. J. Duan, H.C. Man, T.M. Yue, J. Phys. D: Appl. Phys. **34**, 2143–2150 (2001)
204. C.-H. Tsai, C.-J. Chien, Opt. Lasers Eng. **41**, 189–204 (2004)
205. J.B. Bernstein, Joo-Han-Lee, Gang-Yang, T.A. Dahmas, IEEE Trans. Semicond. Manuf. **13**, 228–234 (2000)
206. S.L. Chen, J. Eng. Manuf. **212**, 113–128 (1998)
207. B.S. Yilbas, A.Z. Sahin, Opt. Laser Tech. **27**, 175–184 (1995)
208. Y. Li, W.P. Latham, A. Kar, Opt. Lasers Eng. **35**, 371–386 (2001)
209. I. Belic, J. Stanic, Opt. Laser Technol. **19**, 309–311 (1987)
210. A. Ivarson, J. Powel, J. Kamalu, C. Magnusson, J. Mater. Process. Technol. **40**, 359–374 (1994)
211. J. Wang, W.C.K. Wong, J. Mater. Process. Technol. **95**, 164–168 (1999)
212. H.Y. Zheng, Z.Z. Han, Z.D. Chen, W.L. Chena, S. Yeo, J. Maters. Proc. Technol. **62**, 294–298 (1996)
213. T.M. Yue, W.S. Lau, Mater. Manuf. Process. **11**, 17–29 (1996)
214. H. Huang, H.Y. Zheng, G.C. Lim, Appl. Surf. Sci. **228**, 201–206 (2004)
215. M. Anderson, R. Patwa, Y.C. Shin, Int. J. Mach. Tools Manuf. **46**, 1879–1891 (2006)
216. J.H. Zhang, T.C. Lee, X. Ai, W.S. Lau, J. Mater. Process. Technol. **57**, 304–310 (1996)
217. G. Lu, E. Siores, B. Wang, J. Mater. Process. Technol. **88**, 154–158 (1999)
218. C.-H. Tsai, H.-W. Chen, J. Mater. Process. Technol. **136**, 166–173 (2003)
219. L. Hong, L. Li, C. Ju, Opt. Lasers Eng. **38**, 279–289 (2002)
220. I. Black, K.L. Chua, Opt. Laser Technol. **29**, 193–205 (1997)
221. I. Black, S.A.J. Livingstone, K.L. Chua, J. Maters. Proc. Tech. **84**, 47–55 (1998)
222. P.A. Rebore, Y.C. Shin, F.P. Incropera, Int. J. Mach. Tools Manuf. **44**, 677–694 (2004)
223. R.F. de Graaf, J. Meijer, J. Mater. Process. Technol. **103**, 23–28 (2000)
224. C. Lehane, H.S. Kwok, Appl. Phys A **73**, 45–48 (2001)

225. X. Zhu, D.M. Villeneuve, Y.A. Naumov, S. Nikumb, P.B. Corkum, Appl. Surf. Sci. **152**, 138–148 (1999)
226. N. Katsarakis, E. Chatzitheodoridis, G. Kiriakidis, M.M. Sigalas, C.M. Soukoulis, W.Y. Leung, G. Tuttle, Appl. Phys. Lett. **74**, 3263–3265 (1999)
227. Z. Illyefaalvi-Vitez, Microelectron. Reliab. **41**, 563–570 (2003)
228. P.P. Pronko, S.K. Dutta, J. Squier, J.V. Rudd, D. Du, G. Mourou, Opt. Commun. **114**, 106–110 (1995)
229. S. Nikumb, Q. Chen, C. Li, H. Reshef, H.Y. Zheng, H. Qiu, D. Low, Thin Solid Films **477**, 216–221 (2005)
230. P. Psyllaki, R. Oltra, Mater. Sci. Eng. A **282**, 145–152 (2000)
231. Y.F. Lu, Y.P. Lee, M.S. Zhou, J. Appl. Phys. **83**, 1677–1684 (1998)
232. J. Zhang, K. Sugioka, S. Wada, H. Tashiro, K. Toyoda, Appl. Phys. A **64**, 367–371 (1997)
233. P.A. Molian, *Surface Modification Technologies-An Engineers Guide*, ed. by T.S. Sudarshan, (Marcel Dekker Inc., New York, 1989) p. 421
234. C.W. Draper, J.M. Poate, Inter. Met. Rev. **30**, 85–108 (1985)
235. C.W. Draper, C.A. Ewing, J. Mater. Sci. **19**, 3815–3825 (1984)
236. C.W. Draper, in *Laser and Electron Beam Processing of Materials* eds. by C.W. White, P.S. Peercy, (Academic, New York, 1980), p. 721
237. C.W. White, M.J. Aziz, in *Surface Alloying by Ion, Electron and Laser Beams*, eds. by L.E. Rehn, S.T. Picraux, H. Wiedersich, (ASM, Metals Park, Ohio 1987), p. 19
238. J. Mazumder, J. Metals. **35**, 18–26 (1983)
239. E. Kennedy, G. Byrne, D.N. Collins, J. Mater. Process. Technol. **155–156**, 1855–1860 (2004)
240. K.H. Lo, F.T. Cheng, H.C. Man, Surf. Coat. Technol. **173**, 96–104 (2003)
241. K.H. Lo, F.T. Cheng, C.T. Kwok, H.C. Man, Mater. Lett. **58**, 88–93 (2003)
242. Q.Y. Pan, W.D. Huang, R.G. Song, Y.H. Zhou, G.H. Zhang, Surf. Coat. Technol. **102**, 245–255 (1998)
243. U.K. Mudali, M.G. Pujar, R.K. Dayal, J. Mater. Eng. Perform. **7**, 214–220 (1998)
244. R. Colação, C. Pina, R. Vilar, Scripta Materialia **41**, 715–721 (1999)
245. B.E. Wilde, M. Manohar, C.E. Albright, Mater. Sci. Engg. A **198**, 43–49 (1995)
246. T.M. Yue, Y.X. Wu, H.C. Man, Surf. Coat. Technol. **114**, 13–18 (1999)
247. R. Li, M.G.S. Ferreira, A. Almeida, R. Vilar, K.G. Watkins, M.A. McMahon, W.M. Steen, Surf. Coat. Technol. **81**, 290–296 (1996)
248. N. Hari Prasad, R. Balasubramaniam, J. Mater. Process. Technol. **68**, 117–120 (1997)
249. T.T. Wong, G.Y. Liang, C.Y. Tang, J. Mater. Process. Technol. **66**, 172–178 (1997)
250. Y.B. Liu, J.D. Hu, Z.Y. Cao, P.K. Rohatgi, Wear **206**, 83–86 (1997)
251. K.G. Watkins, Z. Liu, M. McMahon, R. Vilar, M.G.S. Ferreira, Mater.Sci. Eng. A **252**, 292–300 (1998)
252. A. Michaelides, C. Panagopoulos, Surf. Coat. Technol. **57**, 173–177 (1993)
253. D. Dube, M. Fiset, A. Couture, I. Nakatsugawa, Mater. Sci. Eng. A **299**, 38–45 (2001)
254. D. Schippman, A. Weisheit, B.L. Mordike, Surf. Eng. **15**, 23–26 (1999)
255. T.M. Yue, A.H. Wang, H.C. Man, Scripta Mater **38**, 191–198 (1997)
256. G. Abbas, Z. Liu, P. Skeldon, Appl. Surf. Sci. **247**, 347–353 (2005)
257. J. Dutta Majumdar, R. Galun, B.L. Mordike, I. Manna, Mater. Sci. Eng. A **361**, 119–129 (2003)
258. T.M. Yue, Q.W. Hu, Z. Mei, H.C. Man, Mater. Lett. **47**, 165–170 (2001)
259. A. Biswas, L. Li, U.K. Chatterjee, I. Manna, S.K. Pabi, J. Dutta Majumdar, Scripta Materialia **59**, 239–242 (2008)
260. A. Biswas, L. Li, U.K. Chatterjee, I. Manna, J. Dutta Majumdar, Metall. Mater. Trans. A, Phys. Metall. Mater. Sci. **40**, 3001–3008 (2009)
261. J.P. Chu, J.M. Rigsbee, G. Banas, F.V. Lawrence Jr, H.E. Elsayed-Ali, Metall. Mat. Trans. A **26**, 1507 (1995)
262. R. Fabbro, J. Fournier, P. Ballard, D. Devaux, J. Virmont, J. Appl. Phys. **68**, 775 (1990)

263. P. Ballard, J. Fournier, R. Fabbro, J. Frelat, L. Castex, J. De Physique Colloque C **3**(Supplement. 49), C3-401 (1988)
264. A.H. Clauer, C.T. Walters, S.C. Ford, in *Laser in Materials Processing*, ed. by M. Bass, (American Society of Metals, Metals Parks, OH, 1983), p. 7
265. J. Dutta Majumdar, I. Manna, Mater. Sci. Eng. A **267**, 50–59 (1999)
266. A.K. Jain, V.N. Kulkarni, D.K. Sood, Thin Solid Films **70**, 86 1–9 (1981)
267. A. Almeida, M. Anjos, R. Vilar, R. Li, M.G.S. Ferreira, W.M. Steen, K.G. Watkins, Surf. Coat. Technol. **70**, 221–229 (1995)
268. C.H. Tang, F.T. Cheng, H.C. Man, Surf. Coat. Technol. **200**, 2606–2609 (2006)
269. J. Dutta Majumdar, B. Ramesh Chandra, A.K. Nath, I. Manna, Surf. Coat. Technol. **201**, 1236–1242 (2006)
270. W. Aihua, Z. Beidi, T. Zengyi, M. Xianyao, D. Shijun, C. Xudong, Surf. Coat. Technol. **57**, 169–172 (1993)
271. K. Uenishi, K.F. Kobayashi, Intermetallics **7**, 553–559 (1999)
272. J. Dutta Majumdar, I. Manna, Mater. Sci. Eng. A **268**, 216–226, 227–235 (1999)
273. J. Dutta Majumdar, B.L. Mordike, I. Manna, Wear **242**, 18–27 (2000)
274. J. Dutta Majumdar, B.L. Mordike, S.K. Roy, I. Manna, Oxid. Met. **57**, 473–498 (2002)
275. J. Dutta-Majumdar, A. Weisheit, B.L. Mordike, I. Manna, Mater. Sci. Eng. A **266**, 123–134 (1999)
276. I. Manna, W.M. Steen, K.G. Watkins, in *Surface Engineering in Materials Science I Conference Proceedings*, eds. by S. Seal, N.B. Dahotre, J.J. Moore, B. Mishra, (TMS, Warrendale, PA, 2000), PP. 377–384, 15086–7528
277. A.H. Wang, T.M. Yue, Compos. Sci. Technol. **61**, 1549–1554 (2001)
278. S. Ignat, P. Sallamand, D. Grevey, M. Lambertin, Appl. Surf. Sci. **225**, 124–134 (2004)
279. J. Dutta Majumdar, B.L. Mordike, R. Galun, I. Manna, Lasers Eng. **12**, 147–170 (2002)
280. F.T. Cheng, C.T. Kwok, H.C. Man, Surf. Coat. Tech. **139**, 14–24 (2001)
281. X.L. Wu, Y.S. Hong, Metal. Mater. Trans. A. **31**, 3123–3127 (2000)
282. A. Agarwal, N.B. Dahotre, Wear. **240** 144–151 (2000); A. Agarwal, N.B. Dahotre, Metal. Mater. Trans. A, **31** 401–408 (2000)
283. S. Tondur, T. Schnick, L. Pawlowski, B. Wielage, S. Steinhäuser, L. Sabatier, Surf. Coat. Tech. **123**, 247–251 (2000)
284. W. Jiang, P.A. Molian, Surf. Coat. Tech. **135**, 139–149 (2001)
285. E. Gemelli, A. Galerie, M. Caillet, J. Mater. Sci. **31**, 6627–6630 (1996)
286. J. Dutta Majumdar, B. Ramesh Chandra, I. Manna, Tribol. Int. **40**, 146–152 (2007)
287. J.P. Chu, J.M. Rigsbee, G. Banas, H.E. Elsayed-Ali, Mat. Sci. Eng. A **260**, 260–268 (1999)
288. P. Peyre, X. Scherperreel, L. Berthe, C. Carboni, R. Fabbro, G. Be'ranger, C. Lemaître, Mat. Sci. Eng. A **280**, 294–302 (2000)
289. J. Lawrence, L. Li, J. Mat. Process. Technol. **142**, 461–465 (2003)
290. D. Sciti, C. Melandri, A. Bellosi, J. Mat. Sci. **35**, 3799–3810 (2000)
291. M.J.J. Schmidt, L. Li, Appl. Surf. Sci. **168**, 9–12 (2000)
292. B. Stolz, R. Poprawe, Surf. Coat. Technol. **112**, 394–400 (1999)
293. D.H. Lowndes, M. DeSilva, M.J. Godbole, A.J. Pedraza, T. Thundat, R.J. Warmack, Appl. Phys. Lett. **64**, 1791–1793 (1994)
294. W. Wong, K. Chan, K.W. Yeung, K.S. Lau, J. Mat. Process. Technol. **132**, 114–118 (2003)
295. K.P. Adhi, R.L. Owings, T.A. Railkar, W.D. Brown, A.P. Malshe, Appl. Surf. Sci. **218**, 17–23 (2003)
296. F. Huang, Q. Lou, J. Dong, Y. Wei, Appl. Surf. Sci. **174**, 1–6 (2003)
297. V. Drine, H. Niino, J. Pola, A. Yabe, Appl. Phys. A **73**, 527–530 (2001)
298. Q.H. Lu, M. Li, J. Yin, Z.K. Zhu, Z.G. Wang, J. Appl. Poly. Sci. **82**, 2739–2743 (2001)
299. M. Csete, Z. Bor, Appl. Surf. Sci. **133**, 5–16 (1998)
300. A. Hartwig, G. Vitr, V. Schlett, Int. J. Adhes. Adhes. **17**, 373–377 (1997)
301. H. Frerichs, J. Stricker, D.A. Wesner, E.W. Kreutz, Appl. Surface Science. **86**, 405–410 (1995)

- 302. E. Arenholz, J. Heitz, M. Wagner, D. Bzuerle, H. Hibst, A. Hagemeyer, *Appl. Surf. Sci.* **69**, 16–19 (1993)
- 303. H.J. Leamy, S.T.T. Rozgonyi, G.K. Celler, *Appl. Phys. Lett.* **32**, 535–537 (1978)
- 304. P.A. Temple, M.J. Soileau, *IEEE J. Quantum Electron.* **17**, 2067–2072 (1981)
- 305. van H.M. Driel, J.E. Sipe, J.F. Young, *J. Lumin.* **30**, 446–471 (1985)
- 306. C.T. Walters, *Appl. Phys. Lett.* **25**, 696–698 (1974)

Laser-Assisted Fabrication of Materials

Majumdar, J.D.; Manna, I. (Eds.)

2013, XXXII, 488 p., Hardcover

ISBN: 978-3-642-28358-1